PHYSICAL REVIEW B **94**, 035122 (2016)

Electronic structure and x-ray magnetic circular dichroism in A_2FeReO$_6$ (A = Ca, Sr, and Ba) oxides

V. N. Antonov,[1,2] L. V. Bekenov,[1] and A. Ernst[2]
[1] *Institute for Metal Physics, 36 Vernadsky Street, 03142 Kiev, Ukraine*
[2] *Max-Planck Institut für Mikrostrukturphysik, Weinberg 2, D-06120 Halle, Germany*

(Received 22 March 2016; revised manuscript received 23 June 2016; published 11 July 2016)

A systematic electronic structure study of A_2FeReO$_6$ (A = Ba, Sr, and Ca) has been performed by employing the local-spin-density approximation (LSDA) and LSDA+U methods using the fully relativistic spin-polarized Dirac linear muffin-tin orbital band-structure method. We investigated the effects of the subtle interplay between spin-orbit coupling, electron correlations, and lattice distortion on the electronic structure of double perovskites. Ca$_2$FeReO$_6$ has a large distortion in the Fe-O-Re bond, and the electronic structure is mainly determined by electron correlations and lattice distortion. In the Ba-Sr-Ca row, the correlation effects at the Fe site are increased. The correlations at the Re site are small in the Ba- and Sr-based compounds but significant in Ca$_2$FeReO$_6$. Ca$_2$FeReO$_6$ behaves like an insulator only if considered with a relatively large value of Coulomb repulsion $U_{\mathrm{eff}} = 2.3$ eV at the Re site in addition to $U_{\mathrm{eff}} = 3.1$ eV at the Fe site. Ca$_2$FeReO$_6$ possesses a phase transition at 140 K where the metal-insulator transition (MIT) occurs between metallic high-temperature and insulating low-temperature phases. The spin and orbital magnetic moments are linear functions of temperature before and after the MIT but change abruptly at the point of the phase transition. From theoretically calculated magnetocrystalline anisotropy energy (MAE), we found that the easy axis of magnetization for the low-temperature phase is along the b direction, in agreement with experimental data. We found that the major contribution to the MAE is due to the orbital magnetic anisotropy at the Re site. X-ray-absorption spectra and x-ray magnetic circular dichroism at the Re, Fe, and Ba $L_{2,3}$ and Fe, Ca, and O K edges were investigated theoretically in the frame of the LSDA+U method. A qualitative explanation of the x-ray magnetic circular dichroism spectra shape is provided by an analysis of the corresponding selection rules, orbital character, and occupation numbers of individual orbitals. The calculated results are compared with available experimental data.

DOI: 10.1103/PhysRevB.94.035122

I. INTRODUCTION

Colossal magnetoresistance (CMR), a giant decrease of the electrical resistivity under a magnetic field, is a remarkable property that can be applied to spintronic devices. The CMR materials also have potential technological applications to magnetic memory and actuators. CMR has been observed in many ferromagnetic (FM) oxides with Curie temperature (T_c) above room temperature, which can be useful in several research fields, such as, for example, in spin electronics, where the coexistence of high spin polarization of the electrical carriers and high T_c is feasible [1]. Thus, an intense amount of research activity has been devoted in the past decade to compounds such as La$_{0.7}$Sr$_{0.3}$MnO$_0$ ($T_c = 370$ K), CrO$_2$ ($T_c = 410$ K), and Fe$_3$O$_4$ ($T_c = 860$ K) [1].

Recently, double perovskites A_2BB'O$_6$ (A = alkaline earth or rare earth and BB' are heterovalent transition metals such as B = Fe,Cr,Mn,Co,Ni; B' = Mo,Re,W) were established as new CMR materials at a low magnetic field and room temperature [2,3]. They often demonstrate intrinsically complex magnetic structures and a wide variety of physical properties as a consequence of the strong interplay between structure, charge, and spin ordering [4] (see Ref. [5] for a review article on these materials). In particular, the series with B and B' being Fe and Re ions, A_2FeReO$_6$ (A = Ba,Sr,Ca) (AFRO), is very promising due to their rather high values of T_c [6,7]. The Ca-based compound Ca$_2$FeReO$_6$ (CFRO) has an anomalously high T_c, about 540 K [6,8], and Sr$_2$FeReO$_6$ (SFRO) and Ba$_2$FeReO$_6$ (BFRO) possess T_c equal to 400 and 325 K, respectively [9,10]. The Re moments are found to define a periodic FM sublattice that is antiferromagnetically coupled to the Fe 3d moments. The physical properties of these compounds depend strongly on the A type. Among this family, BFRO and SFRO show ferrimagnetic (FiM) and metallic characteristics. On the other hand, CFRO is rather unique: it was revealed to be a paramagnetic metal at T above 538 K, a FiM metal between 538 and 140 K, and a FiM insulator at T below 140 K [6,7,9,11–15].

The crystallographic structure of A_2FeReO$_6$ compounds also depends on the A atom size. The smaller the A cation is, the lower is the symmetry of the unit cell. While BFRO crystallizes in a cubic cell, SFRO has a tetragonal structure. The crystal structure of CFRO was studied by Gopalakrishanan *et al.* [16], Westerburg *et al.* [17], and Oikawa *et al.* [14]. Above 140 K, the compound was found to adopt a monoclinic structure (space group $P2_1/n$), which has a FiM structure with the spin direction along $\langle 001 \rangle$, whereas below this temperature the FiM phase possesses an isomorphous monoclinic structure with different monoclinic angles and the spin direction is along $\langle 010 \rangle$. The change in the octahedral distortion at the metal-insulator transition (MIT) suggests that this structural phase transition may be caused by orbital ordering.

Despite the extensive experimental and theoretical research on the electronic and magnetic structures of AFRO (A = Ba, Sr, and Ca) compounds, some controversies still remain from both theoretical and experimental points of view. From the theoretical side, there is still no clear evidence of the insulating character of CFRO. Several *ab initio* studies have appeared in recent years trying to analyze the electronic structure of CFRO by using different methods and approximations [18].

Up to now, the only way to obtain an insulating state has been to use a rather large value of the Coulomb repulsion U on the Re site [19], something quite rare for a $5d$ ion. From the experimental point of view, some papers have appeared quite recently suggesting that CFRO may not be a complete insulator but just a bad metal [20]. Another discrepancy concerns the phase transition in CFRO at ~ 140 K. Several authors claimed mesoscopic phase separation at low temperature [17,21] with up to three monoclinic phases coexisting below 140 K. Other authors instead suggested the existence of a spin reorientation coupled to a slight change in the local environment of the Fe atom at that temperature [14].

Most of the earlier theoretical works have been devoted to structural, magnetic, and electronic properties [2,11,12,18,19,22–27], while this paper is concentrated on the theoretical investigation of x-ray-absorption spectra (XAS) and x-ray magnetic circular dichroism (XMCD) in AFRO ($A =$ Ca, Sr, and Ba) double oxides. The x-ray-absorption spectroscopy and XMCD in these compounds were carried out by several authors [10,28–32]. Herrero-Martin *et al.* [28] investigated the electronic and geometrical local structures of Re-based double perovskites using x-ray-absorption spectroscopy at the Fe K and Re $L_{1,2,3}$ edges. The measurements have shown a significant sensitivity of the Fe K and Re L_1 edges to the Fe and Re valences, respectively. Winkler *et al.* [31] investigated spin and orbital magnetic moments of the Re $5d$ ion in the double perovskites AFRO by XMCD at the Re $L_{2,3}$ edges. An unusually large negative spin and positive orbital magnetic moment at the Re atoms was detected. They showed also that the usually neglected alkaline earth ions also contribute to the magnetism in these double perovskites.

The energy band structure of AFRO compounds in this paper is calculated within the *ab initio* approach taking into account strong electron correlations by applying the local spin-density approximation to the density-functional theory supplemented by the Hubbard U term (LSDA+U) [33]. The paper is organized as follows. The computational details are presented in Sec. II. Section III presents the electronic structure of AFRO compounds and magnetocrystalline anisotropy in CFRO. Section IV presents the XAS and XMCD spectra of AFMO compounds. Theoretical results are compared with the experimental measurements. Finally, the results are summarized in Sec. V.

II. COMPUTATIONAL DETAILS

A. Crystal structure

Double-ordered AFRO perovskites possess a modified perovskite structure (ABO_3), where the FeO_6 and ReO_6 octahedra are alternatively arranged in two fcc sublattices. This cubic structure can be well described within the $Fm\bar{3}m$ space group. However, this structure is very often distorted as a consequence of pressure or temperature variations.

At room temperature, the crystal structure is cubic ($Fm\bar{3}m$; group number 225) for BFRO, tetragonal ($I4/m$; group number 87) for SFRO, and monoclinic ($P2_1/n$; group number 14) for CFRO [8] (Fig. 1). The oxygen atoms surrounding the Fe and Re sites provide an octahedral environment. The structural differences can be understood taking into account a tilting of the Fe/Re-O octahedra. While the A cation size is getting smaller, empty space shows up around it and needs to be filled up. The cubic structure is then replaced by structures exhibiting lower symmetry. Using Glazer's terminology [34], the $a^0a^0c^-$ octahedral tilt is responsible for the occurrence of the $I4/m$ space group, while the $P2_1/n$ space group arises

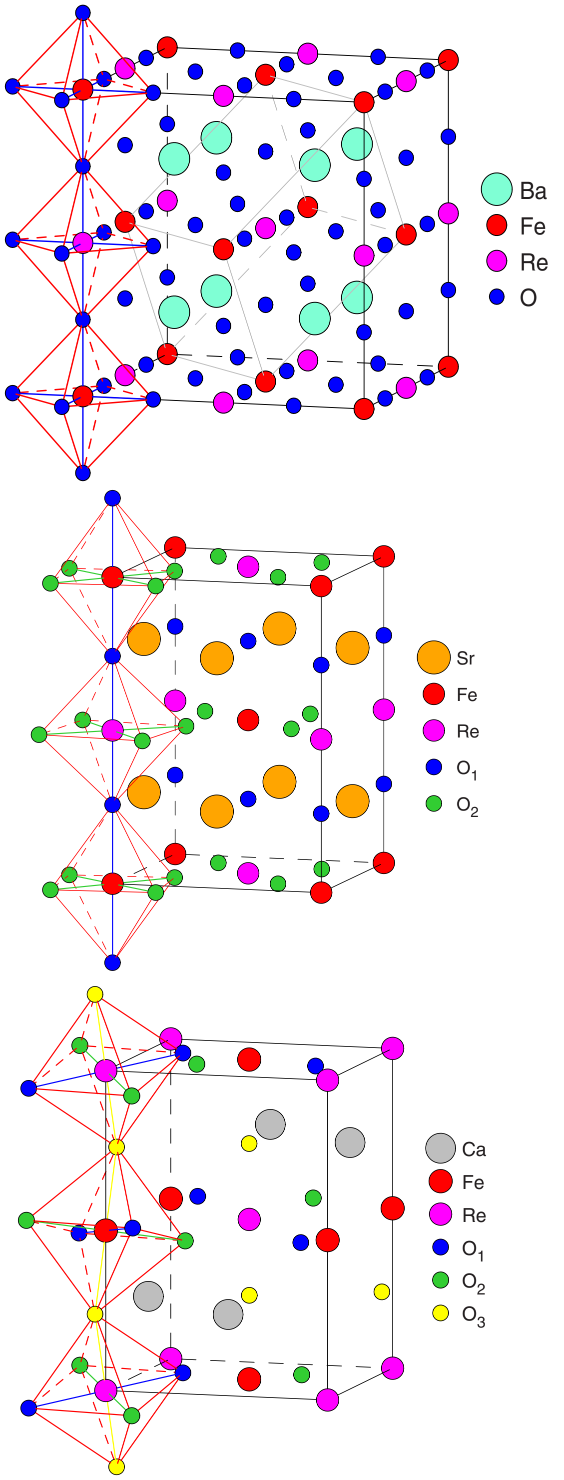

FIG. 1. Upper panel: schematic representation of the $Fm\bar{3}m$ BFRO structure (gray lines show the primitive cell). Middle panel: schematic representation of the $I4/m$ SFRO structure. Lower panel: the primitive cell of the $P2_1/n$ CFRO structure.

TABLE I. Atomic positions of BFRO ($Fm\bar{3}m$) at 30 K (lattice constant $a = 8.0518$) [5], SFRO ($I4/m$) at 1.5 K (lattice constants $a = 5.5425$ Å and $c = 7.9063$ Å) [35], CFRO ($P21/n$) at 7 K (lattice constants $a = 5.390\,23$ Å, $b = 5.516\,48$ Å , $c = 7.671\,91$ Å, and $\beta = 90.2212^\circ$) [14], and CFRO ($P21/n$) at 300 K (lattice constants $a = 5.400\,78$ Å, $b = 5.525\,25$ Å , $c = 7.683\,90$ Å, and $\beta = 90.0695^\circ$) [14].

Compound (Ref.)	Atom	Site	x	y	z
BFRO [5]	Ba	$8c$	0.25	0.25	0.25
	Fe	$4a$	0	0	0
	Re	$4b$	0.5	0.5	0.5
	O	$4e$	0.25	0	0
SFRO [35]	Sr	$4d$	0	0.5	0.25
	Fe	$2a$	0	0	0
	Re	$2b$	0	0	0.5
	O_1	$4e$	0	0	0.2576
	O_2	$8h$	0.2161	0.2718	0
CFRO [14] 7K	Ca	$4e$	0.0102	0.04845	0.2471
	Fe	$2c$	0	0.5	0
	Re	$2d$	0.5	0	0
	O_1	$4e$	0.3033	0.290	0.04420
	O_2	$4e$	0.2926	0.2973	0.45617
	O_3	$4e$	0.5838	−0.02411	0.2463
CFRO [14] 300 K	Ca	$4e$	0.0102	0.04639	0.2479
	Fe	$2c$	0	0.5	0
	Re	$2d$	0.5	0	0
	O_1	$4e$	0.3005	0.2895	0.04430
	O_2	$4e$	0.2918	0.2993	0.45817
	O_3	$4e$	0.58229	−0.02286	0.2452

from the $a^+b^-b^-$ tilt [8]. Basically, two different types of distortion are included in the monoclinic $P2_1/n$ structure of the CFRO oxide shown in the lower panel of Fig. 1. One is a rotating distortion of the FeO_6 and ReO_6 octahedra around the **c** axis, tilting them in alternating directions around the **b** axis so that the Fe-O-Re angle changes from 180° to ∼ 156° ($GdFeO_3$-type distortion) [16]. The second type of crystal distortion in CFRO is a Jan-Teller (JT) distortion driven by the deformation of the FeO_6 and ReO_6 octahedra, which causes different Fe(Re)-O bond lengths. The former distortion is rather weak in CFRO. Moreover, the CFRO sample shows a structural transition (between two monoclinic phases) at about 140 K [6,14,21]. The lattice constants and atomic occupations for all three crystal structures are presented in Table I.

B. Magnetocrystalline anisotropy

Magnetic anisotropy is an important parameter, since it determines the extent to which the magnetization retains its orientation in response to a magnetic field. As the most important magnetic anisotropy term, magnetocrystalline anisotropy is related to the crystal symmetry of a material. The magnetocrystalline anisotropy energy (MAE) describes the tendency of the magnetization to align along specific spatial directions rather than to randomly fluctuate over time. Whereas the exchange interaction among electron spins is purely isotropic, the orbital magnetization, via the spin-orbit interaction, connects the spin magnetization to the atomic structure of a magnetic material, hence giving rise to magnetic anisotropy [36]. It should be noted that for systems with strong structural anisotropy, one may have effective anisotropic exchange among spins in a lattice mediated by the anisotropic interaction among localized and delocalized orbitals.

The calculation of the magnetocrystalline anisotropy energy has been a long-standing problem. At early stage it was treated in a perturbative way [37,38]. Recent investigations elaborated the MAE problem using *ab initio* calculated energy bands obtained within the local-spin density approximation [39–41]. The calculation of the MAE from first principles poses a great computational challenge. The prime obstacle is the smallness of the MAE, which is only a few meV/at, a value that ought to result as the difference of two total energies for different magnetization directions, which are both of the order of 4×10^4 eV/at. Due to this numerical problem, it was unclear at first whether the LSDA could describe the MAE correctly, since a wrong easy axis was obtained for hcp Co and fcc Ni [42]. Recent contributions were aimed at improving the numerical techniques [39,40,43], and the correct easy axis was obtained for hcp Co [39], bcc Fe and fcc Co [40], as well as for some other complex compounds [44–46].

For the material exhibiting uniaxial anisotropy, such as a hexagonal or tetragonal crystal, the MAE can be expressed as [47]

$$\begin{aligned} K = {} & K_1 \sin^2\theta + K_2 \sin^4\theta + K_3^{'} \sin^6\theta \\ & + K_3 \sin^2\theta \cos[6(\phi + \psi)] + \cdots , \end{aligned} \tag{1}$$

where K_i is the anisotropy constant of the ith order, θ and ϕ are the polar angles of the Cartesian coordinate system, where the c axis coincides with the z axis (the Cartesian coordinate system was chosen such that the x axis is rotated through 90° with respect to the hexagonal axis), and ψ is a phase angle.

Both the dipolar interaction and the spin-orbit coupling give rise to the MAE, the former contributing only to the first-order constant K_1. Hear, we deal with the MAE caused only by the spin-orbit interaction. Both magneto-optical effects and the MAE have a common origin in the spin-orbit coupling and exchange splitting. Thus, a close connection between the two phenomena seems plausible. In this paper, the MAE is defined as the difference between two self-consistently calculated fully relativistic total energies for two different crystallographic directions, $K = E(\theta,\phi) - E_{\langle 001 \rangle}$.

C. X-ray magnetic circular dichroism

Magneto-optical (MO) effects refer to various changes in the polarization state of light upon interaction with materials possessing a net magnetic moment, including rotation of the plane of linearly polarized light (Faraday, Kerr rotation), and the complementary differential absorption of left and right circularly polarized light (circular dichroism). In the near-visible spectral range, these effects result from excitation of electrons in the conduction band. Near x-ray-absorption edges, or resonances, magneto-optical effects can be enhanced by transitions from well-defined atomic core levels to transition symmetry-selected valence states.

Within the one-particle approximation, the absorption coefficient $\mu_j^{\lambda}(\omega)$ for incident x-ray of polarization λ and photon energy $\hbar\omega$ can be determined as the probability of electronic transitions from initial core states with the total angular momentum j to final unoccupied Bloch states,

$$\mu_\lambda^j(\omega) = \sum_{m_j} \sum_{n\mathbf{k}} |\langle \Psi_{n\mathbf{k}} | \Pi_\lambda | \Psi_{jm_j} \rangle|^2 \delta(E_{n\mathbf{k}} - E_{jm_j} - \hbar\omega) \times \theta(E_{n\mathbf{k}} - E_F), \tag{2}$$

where Ψ_{jm_j} and E_{jm_j} are the wave function and the energy of a core state with the projection of the total angular momentum m_j; $\Psi_{n\mathbf{k}}$ and $E_{n\mathbf{k}}$ are the wave function and the energy of a valence state in the nth band with the wave vector $\mathbf{k}$; and E_F is the Fermi energy.

Π_λ is the electron-photon interaction operator in the dipole approximation,

$$\Pi_\lambda = -e\boldsymbol{\alpha}\mathbf{a}_\lambda, \tag{3}$$

where $\boldsymbol{\alpha}$ are the Dirac matrices and $\mathbf{a}_\lambda$ is the λ polarization unit vector of the photon vector potential, with $a_\pm = 1/\sqrt{2}(1, \pm i, 0), a_\parallel = (0,0,1)$. Here, + and − denote, respectively, left and right circular photon polarizations with respect to the magnetization direction in the solid. Then, x-ray magnetic circular and linear dichroisms are given by $\mu_+ - \mu_-$ and $\mu_\parallel - (\mu_+ + \mu_-)/2$, respectively. More detailed expressions of the matrix elements in the electric dipole approximation may be found in Refs. [48–51]. The matrix elements due to magnetic dipole and electric quadrupole corrections are presented in Ref. [51].

Concurrent with the development of the x-ray magnetic circular dichroism experiment, some important magneto-optical sum rules have been derived [52–55].

For the $L_{2,3}$ edges, the l_z sum rule can be written as [50]

$$\langle l_z \rangle = n_h \frac{4}{3} \frac{\int_{L_3+L_2} d\omega(\mu_+ - \mu_-)}{\int_{L_3+L_2} d\omega(\mu_+ + \mu_-)}, \tag{4}$$

where n_h is the number of holes in the d band, $n_h = 10 - n_d$, and $\langle l_z \rangle$ is the average of the magnetic quantum number of the orbital angular momentum. The integration is taken over the whole $2p$ absorption region. The s_z sum rule can be written as

$$\langle s_z \rangle + \frac{7}{2}\langle t_z \rangle = n_h \frac{\int_{L_3} d\omega(\mu_+ - \mu_-) - 2\int_{L_2} d\omega(\mu_+ - \mu_-)}{\int_{L_3+L_2} d\omega(\mu_+ + \mu_-)}, \tag{5}$$

where t_z is the z component of the magnetic dipole operator $\mathbf{t} = \mathbf{s} - 3\,\mathbf{r}\,(\mathbf{r}\cdot\mathbf{s})/|\mathbf{r}|^2$, which accounts for the asphericity of the spin moment. The integration $\int_{L_3}$ ($\int_{L_2}$) is taken only over the $2p_{3/2}$ ($2p_{1/2}$) absorption region.

D. Calculation details

The details of the computational method are described in our previous papers [56,57], and here we only mention some aspects specific to the present calculations. The calculations were performed using the spin-polarized fully relativistic linear muffin-tin orbital (LMTO) method [58–60] for the experimentally observed lattice constants [61]. The basis consisted of the s, p, and d LMTO's for Ba, Sr, and O sites, and the s, p, d, and f LMTO's for Ca, Fe, and Mo sites. The $\mathbf{k}$-space integrations were performed with the improved tetrahedron method [62], and the self-consistent charge density was obtained with 518, 554, and 882 irreducible $\mathbf{k}$ points for CFRO, SFRO, and BFRO compounds, respectively.

The x-ray-absorption and dichroism spectra were calculated taking into account the exchange splitting of core levels. The finite lifetime of a core hole was accounted for by folding the spectra with a Lorentzian. The widths of core-level spectra Γ_{L_2}, Γ_{L_3}, and K for Fe, Re, Ca, and O were taken from Ref. [63]. The finite apparative resolution of the spectrometer was accounted for by a Gaussian of width 0.6 eV.

It is well known that the LSDA fails to describe the electronic structure and properties of the systems in which the interaction among the electrons is strong. In recent years, more advanced methods of electronic structure determination, such as the LSDA plus self-interaction corrections [64], the LSDA+U [33] method, the GW approximation [65], and dynamical mean-field theory [66–68], have sought to remedy this problem and have shown considerable success. Among them, the LSDA+U method is the simplest and most frequently used. We used the "relativistic" generalization of the rotationally invariant version of the LSDA+U method [69], which takes into account spin-orbit (SO) coupling so that the occupation matrix of localized electrons becomes nondiagonal in spin indexes. This method is described in detail in our previous paper [69], including the procedure to calculate the screened Coulomb U and exchange J integrals, as well as the Slater integrals F^2, F^4, and F^6.

The screened Coulomb U and exchange J integrals enter the LSDA+U energy functional as external parameters and have to be determined independently. These parameters can be determined from supercell LSDA calculations using Slater's transition state technique [70,71], from constrained LSDA calculations (cLSDA) [71–75], or from the constrained random-phase approximation (cRPA) scheme [76]. Subsequently, a combined cLSDA and cRPA method was also proposed [77]. The cRPA method, however, is known to yield values of U that are too small in some cases [45]. On the other hand, the cLSDA method produces too large values of U [78]. For example, Anisimov and Gunnarsson [70] computed the effective on-site Coulomb interaction in metallic Fe and Ce. For Ce, the calculated Coulomb interaction was found to be about 6 eV, in good agreement with empirical and experimental estimates ranging from 5 to 7 eV. The result for Fe (also about 6 eV) was surprisingly high since U was expected to be in the range of 2–3 eV for elemental transition metals [79,80]. We applied the cLSDA method to Ca_2FeReO_6 and obtained $U_{Fe} = 9.43$ eV and $U_{Re} = 5.76$ eV for the Fe and Re sites, respectively. These values are overestimated in comparison with typical Hubbard U values for $3d$ and $5d$ compounds.

The precision values of the Hubbard U for Fe and Re are critical to describe the magnetocrystalline anisotropy and the electronic structure in close proximity to the metal-insulator phase transition in CFRO. Because of the difficulties in obtaining an unambiguous determination of U, it can be considered as a parameter of the model. Its value can therefore be adjusted to achieve the best agreement of the results of LSDA+U calculations with external experimental inputs from the photoemission, x-ray bremsstrahlung isochromat, or

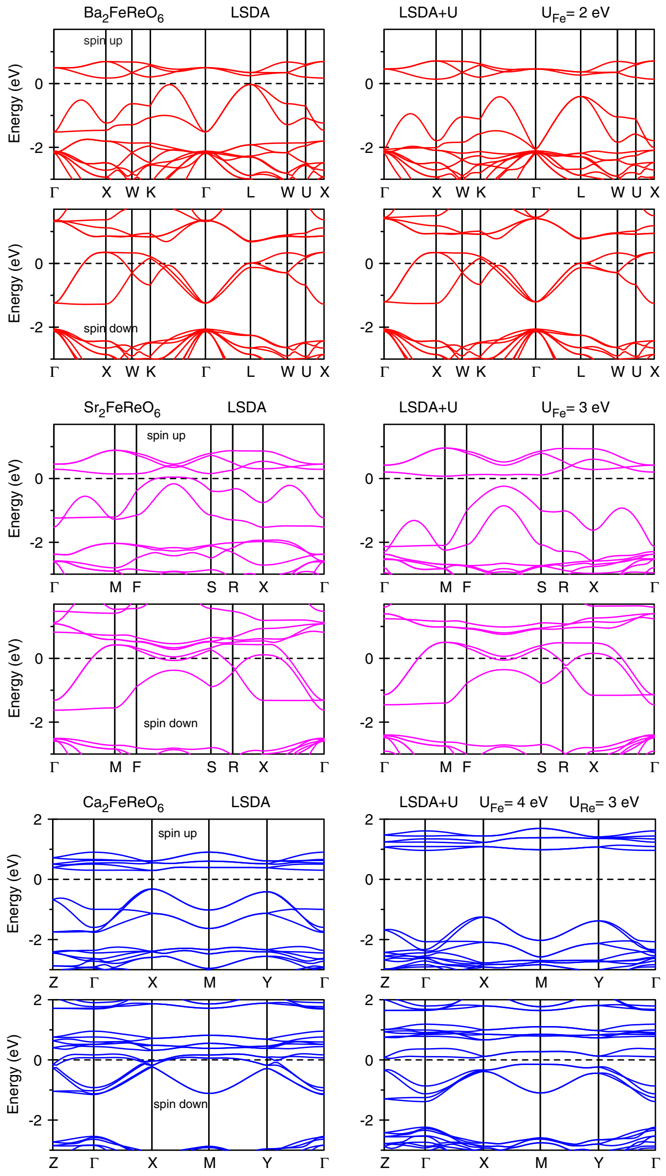

FIG. 2. Energy band structures of BFRO, SFRO, and CFRO calculated in the LSDA (left row) and the LSDA+U (right row) approximations.

optical spectroscopy. We choose for that purpose available experimental optical spectra. We varied the Hubbard U parameter from 1 to 6 eV and found that the set of Hubbard U parameters, $U_{\mathrm{Fe}} = 4$ eV and $U_{\mathrm{Re}} = 3$ eV, shows the best agreement between theory and the optical experiment in CFRO (see Fig. 2 in the supplemental material [81]). The LSDA+U approximation with a small $U_{\mathrm{Fe}} = 2$ eV also slightly improves the agreement between theory and experiment in BFRO in comparison with the LSDA approach (see Fig. 3 in the supplemental material). We choose the following Hubbard U parameters: $U = 2$, 3, and 4 eV at the Fe site for BFRO, SFRO, and CFRO, respectively, and $U_{\mathrm{Re}} = 3$ eV for CFRO. The cLSDA calculations produce $J = 0.9$ and 0.7 eV for the Fe and Re sites, respectively, in AFRO. We fixed these values and use them throughout the paper.

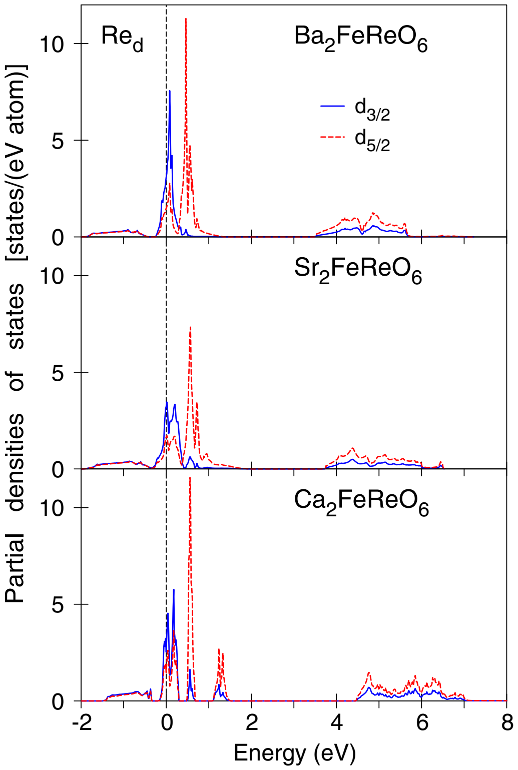

FIG. 3. The Re $5d$ partial DOSs of BFRO, SFRO, and CFRO calculated in the LSDA relativistic Dirac approximation.

III. ELECTRONIC STRUCTURE

A. Energy bands

Generally in $3d$ transition-metal oxides (TMOs), the SO coupling is typically less than 0.05 eV. This is much smaller than other important energies in $3d$ TMOs, such as the on-site Coulomb interaction energy, U (3–5 eV), and the crystal-field splitting energy, Δ (2–3 eV). Therefore, the SO coupling is not dominant in determining the physical properties of $3d$ TMOs. On the other hand, in $5d$ TMOs, the SO coupling is approximately 0.3–0.5 eV [82], and therefore it should be taken into account when describing the electronic structure of $5d$ TMOs [26].

We start with a review of the basic electronic and magnetic properties of the compounds using the standard LSDA approximation. Figure 2presents the energy band structures of BFRO, SFRO, and CFRO calculated in the LSDA (left row). The LSDA approach produces the half-metallic state in BFRO where the only contribution around the Fermi level comes from the minority spins. There is an energy gap of 0.20 eV between the Fe e_g and Re t_{2g} states in the spin-up channel. The total spin magnetic moment is equal to $3\mu_{\mathrm{B}}$ in the spin-polarized calculation (without taking into account the SO coupling), which is consistent with the expected half-metallic nature of this compound. The half-metallic gap and SO splitting are of the same order in BFRO, therefore SO coupling destroys the half-metallic property by introducing a minor density of states of Re at the Fermi energy level in the insulating channel. A similar conclusion was derived in previous theoretical calculations [26].

The LSDA approach is not able to produce a half-metallic solution in SFRO. However, such a solution can be obtained in the frame of the LSDA+U approximation with $U = 3$ eV ($U_{\text{eff}} = U - J = 2.1$ eV) applied to the Fe $3d$ states (see the right column of Fig. 2).

Photoemission spectroscopy measurements show that small spectral weight at the Fermi level observed above the MIT temperature gradually disappears with decreasing T, forming a small ($\leqslant 50$ meV) energy gap [83]. The LSDA is not able to create a finite gap, and consequently it cannot explain the semiconducting behavior for CFRO. The Hubbard $U =$ 3–6 eV applied only to Fe $3d$ orbitals shifts progressively the Fe $3d$ states away from the Fermi level, reducing the hybridization between Fe and Re orbitals but without any remarkable changes in the metallicity or band fillings (see Fig. 1 in the supplemental material).

Now, we are going to analyze possible correlation effects on Re sites. Re $5d$ orbitals are quite extended, so correlations are expected to be rather small in the Re $5d$ shell. However, a pure insulating behavior shows up in CFRO only when the Hubbard U is applied also to the Re $5d$ states. A similar conclusion was already achieved in previous publications [19,25,26,83], although, our value of $U_{\text{eff}}^{\text{Re}}$ is the smallest among other publications. Figure 3 presents the LSDA Re $5d$ partial DOSs in Ba-, Sr-, and Ca-based compounds calculated in the fully relativistic Dirac approximation. It is clearly seen that the Re bandwidth in CFRO is significantly smaller than that in other two compounds, which should yield strong electron correlations in the Re $5d$ bands in the Ca-based oxide. The CFRO band structure shows rather narrow bands near the Fermi level with pseudogaps immediately above it. These band separations almost disconnect states with dominant Fe contributions, above the Fermi level, from the Re bands. A similar situation occurs for the Fe $3d$ energy bands. We found that the Fe t_{2g} bandwidth is reduced by approximately 25% coming from Sr- to Ca-based compounds. The difference in Fe and Re d bandwidths between Ba, Sr, and Ca compounds can be understood on the basis of the difference in their crystal distortion. The degree of GdFeO$_3$-type and JT distortions is increased in the series of double perovskites A_2FeReO$_6$ ($A =$ Ba, Sr, and Ca). The Fe-O-Re bond angle in CFRO with a monoclinic structure is $\sim 156^\circ$ [16], whereas it is 180° in cubic BFRO and tetragonal SFRO. The deviation of the Fe-O-Re bond angle from 180° reduces the Fe-Re overlap and narrows the t_{2g} bandwidths. In addition, CFRO induces monoclinic distortion, which lifts the degeneracy of the t_{2g} levels on the Fe and Re sites. These two factors lead to more narrow Fe and Re t_{2g} energy bands in the Ca compound, in comparison with Ba- and Sr-based ones. We can conclude that under the influence of an increasing GdFeO$_3$-type distortion, the Fe and Re t_{2g} electrons become increasingly localized and CFRO undergoes a Mott transition.

The effect of GdFeO$_3$ -type and Jahn-Teller distortions on the degree of d-electron localization was investigated by Pavarini *et al.* [84] for the series of orthorhombic perovskites ABO$_3$ = SrVO$_3$, CaVO$_3$, LaTiO$_3$, and YTiO$_3$. The B t_{2g} states under the influence of the increasing GdFeO$_3$-type and JT distortions become increasingly localized. This manifests in a significant decrease of the width of the $3d$ energy bands. Through the series, the increasing misalignment of the xy, yz, and zx orbitals and the theft of the O p character by the A ions lead to a decrease of the t_{2g} bandwidth by about 50%. In addition, a Mott transition occurs between CaVO$_3$ and LaTiO$_3$. These results are also in accord with those obtained from studies of model Hamiltonians by Mochizuki and Imada [85,86].

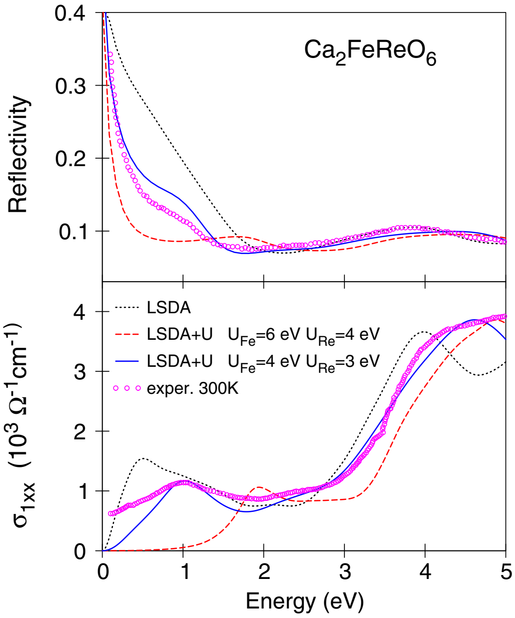

FIG. 4. Experimentally measured reflectivity (upper panel) and optical conductivity (lower panel) [26] at 300 K (open magenta circles) in CFRO in comparison with the theoretical spectra in the LSDA and LSDA+U approximations.

For a series of adopted Hubbard U values in this study, our calculations show that the properties of the ground state as well as XAS and XMCD spectra are not sensitive to the choice of U. The XMCD spectra have almost the same shape, with U varying by ± 1 eV (see Figs. 4 and 5 in the supplemental material). On the other hand, the energy gap and optical spectra are very sensitive to the precise value of U. Figure 4 shows the experimentally measured reflectivity at 300 K (upper panel) and the optical conductivity $\sigma(\omega)$ (lower panel) in CFRO [26] in comparison with the theoretical spectra in the LSDA and LSDA+U approximations. The experimental optical conductivity spectrum possesses three major peaks at 1, 2.3, and 4–5 eV. The set of Hubbard U parameters $U_{\text{Fe}} = 4$ eV and $U_{\text{Re}} = 3$ eV in the LSDA+U approach shows the best agreement between the theory and the optical experiment (see Fig. 2 in the supplemental material). The LSDA as well as the LSDA+U with larger values of U fail to describe the correct position of major optical conductivity peaks. One should mention that the optical conductivity spectrum measured at room temperature (300 K) presented in Fig. 4 has a finite optical conductivity value in close proximity to zero frequency. The same authors also measured $\sigma(\omega)$ within the 0–0.5 eV energy interval below the MIT at 10 K [26]. The low-temperature spectrum $\sigma(\omega) \to 0$ if $\omega \to 0$, in agreement with our LSDA+U calculations.

We found that, although the LSDA approach describes relatively well the optical spectra of BFRO, the LSDA+U

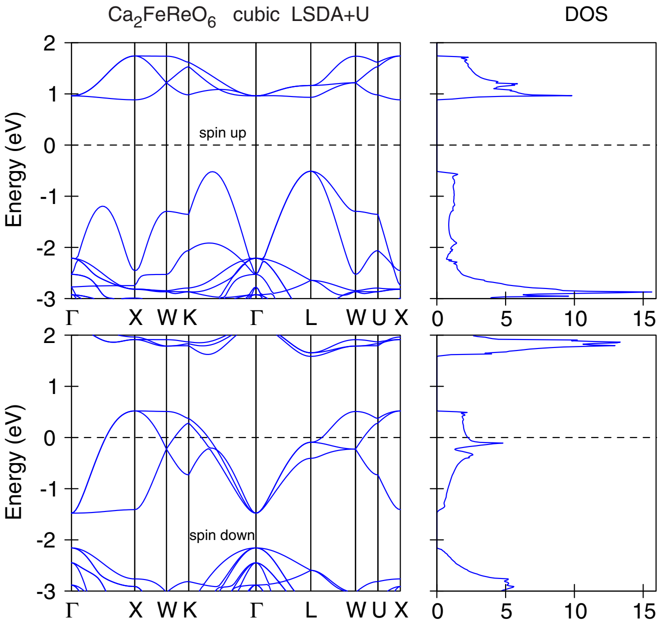

FIG. 5. Energy band structure of CFRO calculated in the LSDA+U approximation without structure distortions.

approximation with small $U = 2$ eV still slightly improves the agreement between theory and experiment (see Fig. 3 in the supplemental material). Therefore, we choose the following LSDA+U parameters: $U_{\text{Fe}} = 2$ eV ($U_{\text{eff}} = 1.1$ eV) for BFRO, $U_{\text{Fe}} = 3$ eV ($U_{\text{eff}} = 2.1$ eV) for SFRO, and $U_{\text{Fe}} = 4$ eV ($U_{\text{eff}} = 3.1$ eV) and $U_{\text{Re}} = 3$ eV ($U_{\text{eff}} = 2.3$ eV) for CFRO. We fixed these values and use them throughout the rest of the paper.

B. Metal-insulator transition in Ca_2FeReO_6

Our results show that CFRO behaves as an insulator only if considered with a relatively large value of Coulomb repulsion $U_{\text{eff}} = 2.3$ eV at the Re site in addition to $U_{\text{eff}} = 3.1$ eV at the Fe site. We found that the band dispersion does not change significantly when the SO coupling is included. This indicates that the U term is more important than the SO coupling in the determination the electronic structure of CFRO. To understand better the effect of the lattice distortion in CFRO, we performed energy band calculations for the cubic $Fm\bar{3}m$ structure with the angle of the Fe-O-Re bond fixed at 180° (rather than the experimentally determined value of 156°). Figure 5 shows calculated results for this hypothetical structure without lattice distortion. We found that the energy band structure of the hypothetical CFRO is nearly the same as that for BFRO (for the same Hubbard U parameters). This suggests that the lattice distortion is significant in real CFRO. Therefore, both the correlation and the lattice distortion play an important role in CFRO. The actual MIT is probably driven by strong electron correlation coupled with Jahn-Teller distortion.

According to neutron powder diffraction (NPD) measurements, structural and magnetic phase transitions in CFRO take place simultaneously at 140 K where the MIT occurs from a metal high-temperature phase with the magnetization along the $\langle 001 \rangle$ direction to an insulator low-temperature phase with magnetization along the $\langle 010 \rangle$ direction [14,21]. Above 140 K, the HT phase was found to adopt a monoclinic structure (space group $P2_1/n$), whereas below this temperature the LT phase possesses an isomorphous monoclinic structure with a different monoclinic angle. The refined structural parameters and angles at 7 and 300 K are summarized in Table I. The interatomic distances d_{ij} of the HT phase can be classified into two long bonds and one short bond in each octahedron. They are equal to 2.025 Å for Fe-$O_{1,2}$ and 1.958 Å for Fe-O_3. The d_{ij} for ReO_6 octahedra are equal to 1.954 Å for Re-$O_{1,2}$ and 1.939 Å for Re-O_3. The interatomic distances of the LT phase are equal to 2.031, 2.012, and 2.004 Å for Fe-O_1, Fe-O_2, and Fe-O_3, respectively, and 1.950, 1.963, and 1.946 Å for Re-O_1, Re-O_2, and Re-O_3, respectively.

Oikawa *et al.* [14] presented a variation of lattice constants and the angle β as a function of temperature. The average bond angle, Fe-O-Re, has a linear temperature dependence in the HT phase, whereas no temperature dependence appeared in the LT phase. At the MIT temperature, there is a change in the distortion direction of ReO_6 octahedra and the interatomic distances d_{ij} in the FeO_6 and ReO_6 octahedra. The abrupt change in the lattice constants and β angle are clearly seen at the MIT point (see Fig. 7 in Ref. [14]), which indicates the phase transition to be of first order.

Figure 6 shows variation of orbital magnetic moments M_l and spin moments M_s at Fe and Re sites as a function of temperature. Here we used the temperature dependence of the lattice constants a, b, and c and angle β obtained by Oikawa *et al.* in Ref. [14]. The spin and orbital magnetic moments change linearly with temperature before and after the MIT and abruptly at the point of the phase transition. This jump is different for different sites. The spin magnetic moment decreases at the MIT by $0.047\mu_{\text{B}}$ at the Fe site and increases in absolute value by $0.014\mu_{\text{B}}$ at the Re site. The orbital magnetic

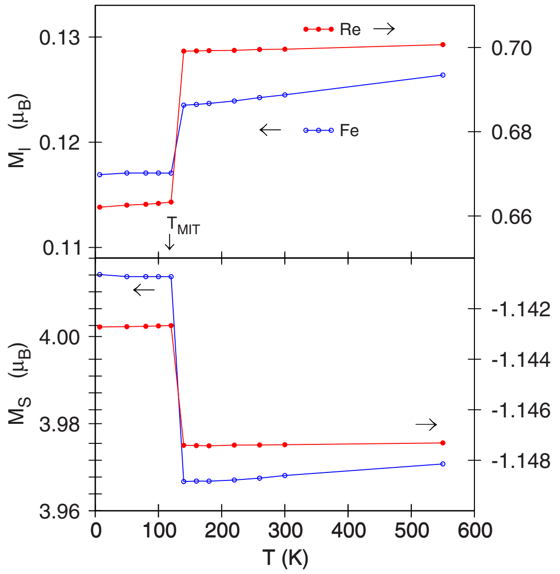

FIG. 6. Variation of orbital magnetic moments M_l (upper panel) and spin moments M_s (lower panel) at the Fe and Re sites in CFRO as a function of temperature. The temperature dependence of the lattice constants and angle β is from Ref. [14].

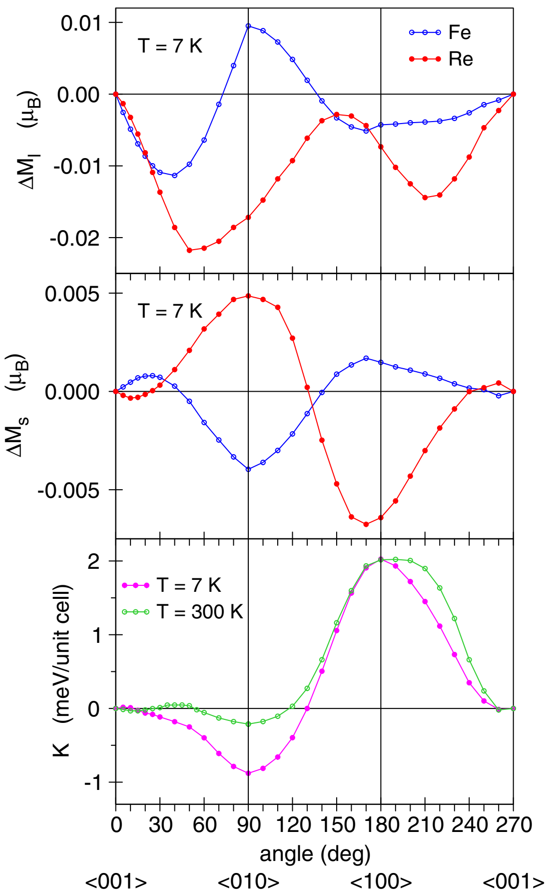

FIG. 7. The MAE (lower panel) for $T = 7$ and 300 K. OMA (ΔM_l) and SMA (ΔM_s) for $T = 7$ K (upper and middle panels, respectively) at the Fe and Re sites.

moments are increased at the MIT for both sites, but the jump in M_l is almost one order of magnitude larger at the Re site than at the Fe one ($0.005\mu_B$ and $0.037\mu_B$, respectively).

Figure 7 (lower panel) shows the MAE as a function of the polar angles θ and ϕ for the HT and LT phases. We found that the easy axis of magnetization for the LT phase is along the b ($\langle 010\rangle$) direction, in agreement with the experimental data [14], with the MAE $K = E_{\langle 010\rangle} - E_{\langle 001\rangle} = -0.88$ meV. For the HT phase, the easy axis of magnetization is still along the $\langle 010\rangle$ direction, which is in contradiction with the experiment, which found the ground state of the HT phase with the spin direction along $\langle 001\rangle$ [14]. Our calculations show two local minima for the HT phase for the $\langle 010\rangle$ direction and close to the $\langle 001\rangle$ direction with canting angle $\theta \sim 10^\circ$ with a small energy barrier in between. Although the $\langle 010\rangle$ direction has lower energy than the $\langle 001\rangle$ direction, the MAE became extremely small in the HT phase, $K = -0.18$ meV (it corresponds approximately to 2 K). Considering such a close competition, it is clear that even a slight degree of chemical disorder and inhomogeneity may change the easy axis of magnetization in the HT phase between the $\langle 010\rangle$ and $\langle 001\rangle$ directions.

Figure 7 also presents the spin magnetic anisotropy (SMA) ΔM_s and orbital magnetic anisotropy (OMA) ΔM_l for $T = 7$ K. The OMA and SMA are larger at the Re site than at the Fe one. The OMA is four times larger than the SMA for both sites. The MAE is proportional to the OMA through expression $K \sim \frac{1}{4}\Lambda_{\mathrm{SO}}\Delta M_l$ [87,88], where Λ_{SO} is the SO parameter. The SO constant $\Lambda_{\mathrm{SO}} \sim 0.04$ eV for $3d$ Fe, but $\Lambda_{\mathrm{SO}} \sim 0.5$ eV for Re [89]. Therefore, the major contribution to the MAE is due to the OMA at the Re site.

IV. XMCD SPECTRA

A. Re, Fe, and Ba $L_{2,3}$ XMCD spectra

Figure 8 shows the calculated XAS and XMCD spectra at the Re $L_{2,3}$ edges in AFRO (A = Ca, Sr, and Ba) oxides together with the experimental spectra. The Re L_3 spectra

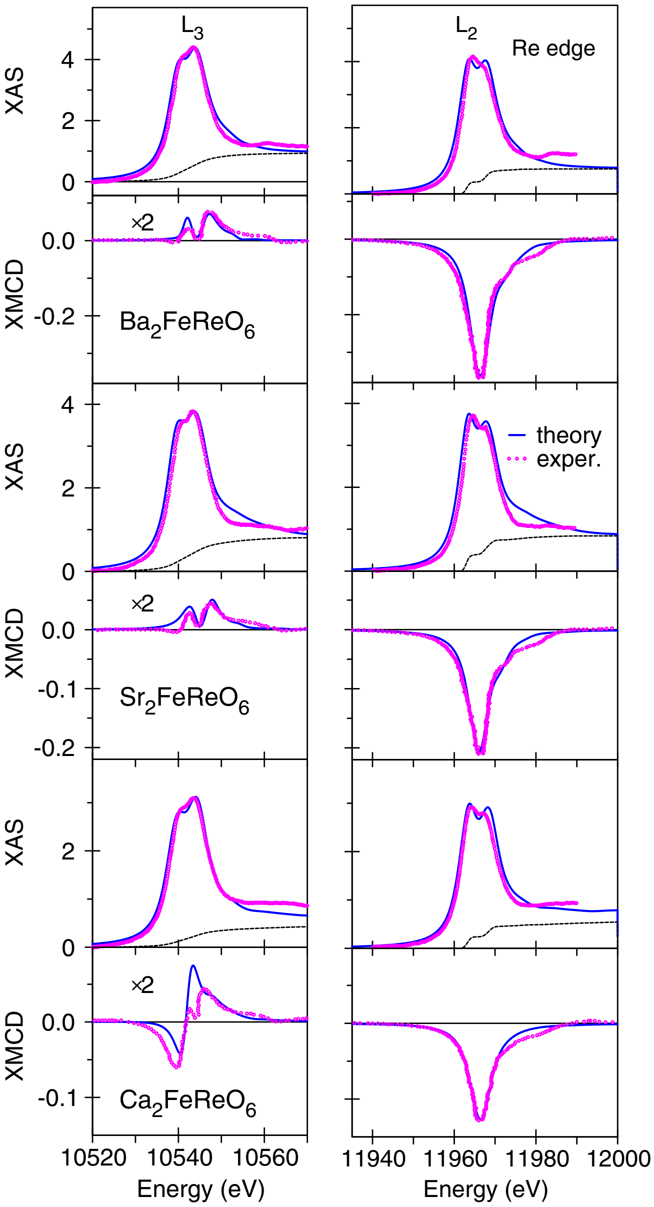

FIG. 8. The experimental x-ray-absorption spectra [28] and XMCD spectra [31] (open circles) at the Re $L_{2,3}$ edges in BFRO, SFRO, and CFRO compared with the theoretically calculated ones. The experimental and theoretically calculated dichroism at the Re L_2 edge is multiplied by a factor of 2.

($2p_{3/2} \rightarrow 5d_{3/2,5/2}$ transitions) have a strong resemblance to each other and the same edge energy position with a double-peak structure. The first maximum appears at about 10 540.1 eV and the second stronger peak is located 3.5 eV above in all the spectra. The energy splitting is generally ascribed to the crystal-field splitting of d orbitals into t_{2g} and e_g states [90]. The Re L_2 x-ray-absorption spectra also have a double-peak structure, however their low-energy peak is more intensive than the high-energy peak. Theory correctly reproduces the energy position and inverse relative behavior of intensity in the L_3 and L_2 XASs.

The experimentally measured dichroic L_2 line consists of a simple asymmetric negative peak with a high-energy shoulder in all the oxides under consideration. The dichroic line at the L_3 edge has three peaks: two positive high-energy peaks and a lower-energy negative peak. This negative peak appears as a low-energy shoulder in BFRO and SFRO compounds and has a rather large intensity in CFRO. The dichroism at the L_2 edge is significantly larger than at the L_3 edge in all three compounds.

A qualitative explanation of the XMCD spectra shape is provided by the analysis of the corresponding selection rules, orbital character, and occupation numbers of individual $5d$ orbitals. Because of the electric dipole selection rules ($\Delta l = \pm 1$; $\Delta j = 0, \pm 1$), the major contribution to the absorption at the L_2 edge stems from the transitions $2p_{1/2} \rightarrow 5d_{3/2}$ and that at the L_3 edge originates primarily from $2p_{3/2} \rightarrow 5d_{5/2}$ transitions, with a weaker contribution from $2p_{3/2} \rightarrow 5d_{3/2}$ transitions.

The selection rules for the magnetic quantum number m_j (m_j is restricted to $-j, \ldots, +j$) are $\Delta m_j = +1$ for $\lambda = +1$ and $\Delta m_j = -1$ for $\lambda = -1$. Table II presents the dipole-allowed transitions for x-ray-absorption spectra at the L_3 and L_2 edges for left ($\lambda = +1$) and right ($\lambda = -1$) polarized x rays.

To go further, we need to discuss the character of the $5d$ empty DOS. Since l and s prefer to couple antiparallel for less than half-filled shells, the $j = l - s = 3/2$ level has a lower energy than the $j = l + s = 5/2$ level. Due to the intra-atomic exchange interaction, the lowest sublevel of $j = 3/2$ will be $m_{3/2} = -3/2$, however for $j = 5/2$ the lowest sublevel will be $m_{5/2} = +5/2$. This reversal in the energy sequence arises from the gain in energy due to alignment of the spin with the exchange field.

TABLE II. The dipole-allowed transitions from core $2p_{1/2,3/2}$ levels to unoccupied $5d_{3/2,5/2}$ valence states for left ($\lambda = +1$) and right ($\lambda = -1$) polarized x rays.

Edge	$\lambda = +1$	$\lambda = -1$
L_3 $2p_{3/2} \rightarrow 5d_{5/2}$	$-3/2 \rightarrow -1/2$	$-3/2 \rightarrow -5/2$
	$-1/2 \rightarrow +1/2$	$-1/2 \rightarrow -3/2$
	$+1/2 \rightarrow +3/2$	$+1/2 \rightarrow -1/2$
	$+3/2 \rightarrow +5/2$	$+3/2 \rightarrow +1/2$
L_3 $2p_{3/2} \rightarrow 5d_{3/2}$	$-3/2 \rightarrow -1/2$	$-1/2 \rightarrow -3/2$
	$-1/2 \rightarrow +1/2$	$+1/2 \rightarrow -1/2$
	$+1/2 \rightarrow +3/2$	$+3/2 \rightarrow +1/2$
L_2 $2p_{1/2} \rightarrow 5d_{3/2}$	$-1/2 \rightarrow +1/2$	$-1/2 \rightarrow -3/2$
	$+1/2 \rightarrow +3/2$	$+1/2 \rightarrow -1/2$

From our band-structure calculations, we found that Re $5d_{3/2}$ states with $m_j = -3/2$ and $-1/2$ are occupied in the AFRO oxides. For the $5d_{5/2}$ states, the $m_j = 5/2$ and $3/2$ states are occupied. Therefore, for the Re L_2 XMCD spectrum, the dipole-allowed transitions are only $-1/2 \rightarrow +1/2$ and $+1/2 \rightarrow +3/2$ for $\lambda = +1$ (Table II). The $-1/2 \rightarrow -3/2$ and $+1/2 \rightarrow -1/2$ transitions are forbidden for $\lambda = -1$ because the $5d_{3/2}$ states with $m_j = -3/2$ and $-1/2$ are occupied. Thus the XMCD spectrum of Re at the L_2 edge ($I = \mu^- - \mu^+$) can be roughly approximated by the following sum of m_j-projected partial densities of states: $-(N^{3/2}_{1/2} + N^{3/2}_{3/2})$. Here we use the notation $N^{j}_{m_j}$ for the density of states with the total momentum j and its projection m_j. As a result, the shape of the Re L_2 XMCD spectrum contains an asymmetric negative peak.

A rather different situation occurs in the case of the L_3 XMCD spectrum. For $2p_{3/2} \rightarrow 5d_{5/2}$, the dipole-allowed transitions $+1/2 \rightarrow +3/2$ and $+3/2 \rightarrow +5/2$ for $\lambda = +1$ are forbidden because the $5d_{5/2}$ states with $m_j = 5/2$ and $3/2$ are occupied. The transitions with the same final states $m_j = -1/2$ and $+1/2$ mostly cancel each other. For $2p_{3/2} \rightarrow 5d_{3/2}$, the transitions $-3/2 \rightarrow -1/2$ for $\lambda = +1$ and $-1/2 \rightarrow -3/2$ and $+1/2 \rightarrow -1/2$ for $\lambda = -1$ are also forbidden because the $5d_{3/2}$ states with $m_j = -3/2$ and $-1/2$ are occupied. The transitions $-1/2 \rightarrow +1/2$ and $+3/2 \rightarrow +1/2$ for $\lambda = +1$ and -1, respectively, mostly cancel each other because they have the same final state $m_j = +1/2$. Therefore, the XMCD spectrum of Re at the L_3 edge can be roughly approximated by the following sum of m_j-projected partial densities of states: $(N^{5/2}_{-5/2} + N^{5/2}_{-3/2}) - N^{3/2}_{3/2}$. From this expression, one would expect two positive peaks and one negative peak in the L_3 XMCD spectrum. This is exactly what we observe in the experimental L_3 XMCD spectra (see the left column in Fig. 8). The energy position and peak intensities are very sensitive to the relative energy positions and intensities of these three partial DOSs.

We should note, however, that the explanation of the XMCD line shape in terms of m_j-projected DOS's presented above should be considered as only qualitative. First, there is no full compensation between transitions with the same final states due to a difference in the angular matrix elements; second, in our consideration we neglect cross terms in the transition matrix elements. In addition, we have used here the jj-coupling scheme; however, the combination of the hybridization, Coulomb, exchange, and crystal-field energies may be so large relative to the $5d$ spin-orbit energy that the jj-coupling is no longer an adequate approximation. Furthermore, the number of Re $5d$ valence electrons is not exactly four but larger. Therefore, some amount of Re $5d_{5/2}$ and $5d_{3/2}$ states, which we have been considering as fully empty, are partially occupied. The occupation numbers of Re $5d_{5/2}$ states are changed insignificantly in the row of Ba-Sr-Ca-based oxides being equal to 2.25, 2.25, and 2.24 in BFRO, SFRO, and CFRO, respectively (Fig. 3). The occupation numbers of Re $5d_{3/2}$ states are changed as 2.08, 2.04, and 2.00, respectively. Therefore, the ionicity is increased in this row.

It is interesting to note that the relative intensity of three peaks of the XMCD spectra at the Re L_3 edge is strongly changed going from Ba to Ca oxides. The high-energy positive peak is the largest in BFRO and becomes smaller in SFRO and CFRO. The low-energy negative peak is the smallest in BFRO and increases significantly in CFRO (see the left column of Fig. 8). The latter can be explained by a decrease in the Re $5d_{3/2}$ occupation number in the Ba-Sr-Ca row, and, hence, an increase in the number of empty $5d_{3/2}$ states (an increase in the contribution from the negative $-N_{3/2}^{3/2}$ term).

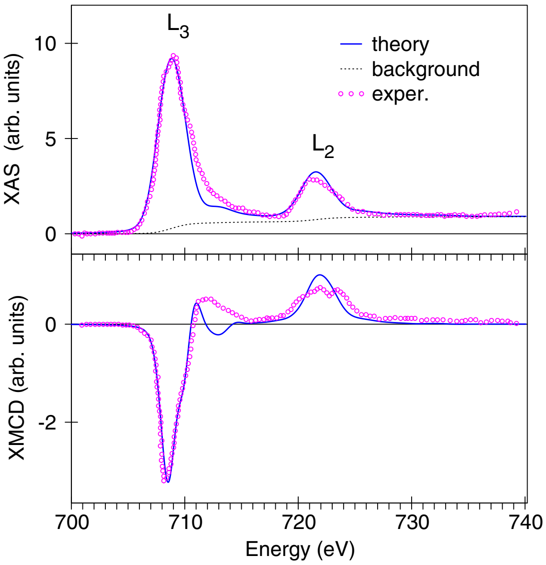

FIG. 9. The experimentally measured x-ray-absorption spectra (upper panel) and XMCD spectra (lower panel) at the Fe $L_{2,3}$ edges in BFRO [10] compared with the theoretically calculated ones.

To calculate the $L_{2,3}$ XAS and XMCD spectra of AFRO compounds, we used a single-particle approximation. It is widely believed that the XAS and XMCD spectra of correlated systems are better described by means of the single-impurity Anderson model (SIAM) [91–98]. Recently, however, it has been argued that for systems with strong hybridization between valence states, calculations based on density-functional theory (DFT) may provide an equally good or even better description of the XAS and XMCD spectra than the SIAM analysis [50,99,100]. The electronic structure obtained from DFT calculations is often compared with photoemission, optical, or XMCD data, and good agreement between the experiment and calculations is frequently observed. In the limit of complete screening of the excited state, one would expect ground-state density-functional calculations to be able to describe the spectra well. One should mention that both the band-structure approach and the atomiclike SIAM have their own advantages and restrictions. To some extent they are complimentary. The band-structure methods more precisely describe the energy band structure of empty conduction states, especially in the case of $5d$ states, which definitely possess band character and extend over more than 15 eV. In addition, the band-structure approach has no adjustable parameters and can be considered as a "first-principles" approach. On the other hand, the SIAM more naturally and more correctly describes the multiplet structure of the final states with a core hole in strongly correlated $4f$ compounds. The method, however, contains several adjustable parameters (such as the energy of the $4f$ level, ε_{4f}, the Coulomb interaction between $4f$ electrons, U_{ff}, and between $4d$ and $5d$ states, U_{fd}, core hole potentials, U_{fc} and U_{dc}, and a hybridization parameter between $4f$ and conducting states, $V_{l\lambda}$). By a proper choice of these parameters, the shape of the XMCD spectra for some rare-earth compounds were described quite well (see the review paper [98]). In the absence of $4f$ $5d$ hybridization in rare-earth compounds ($4f$ $5d$ hopping is forbidden), there is only one $4f$ configuration final state. The spectral shape of the XAS at the $L_{2,3}$ edge in this case is due to the energy distribution of empty $5d$ states. In the case of nonzero $4f$ $5d$ hybridization, the creation of a core hole in the process of x-ray-absorption leads to a set of final states with different $4f$ occupations. These final states may influence the spectral shape of the XAS and XMCD spectra even if $4f$ states are not involved directly in the x-ray absorption (as in the $L_{2,3}$ absorption). These final states lead to spectral contributions that are shifted energetically from each other. When an x-ray-absorption spectrum is much wider than the $4f$ configuration energy shifts between different configurations, the multiplet structure due to the core-hole effect in rare-earth $L_{2,3}$ XAS manifests only as an additional broadening of the spectra. In this case, one can expect that the band-structure calculations are able to reproduce the XAS and XMCD spectral shape even in the presence of $4f$-$5d$ hybridization. It was shown recently that DFT and the atomiclike SIAM yield very similar results for XMCD spectra at the Yb $L_{2,3}$ edges in the strongly correlated $YbAgCu_4$ compound [101].

In the case of the Re $L_{2,3}$ XAS and XMCD spectra in AFRO compounds, one would expect an even smaller effect of the final-state interaction because the Re $5d$ states are less localized in comparison with the $4f$ states, and they have a smaller amplitude inside the MT sphere. In addition, the width of the Re L_3 x-ray-absorption spectrum is more than 30 eV, which is one order of magnitude larger than the configuration energy shifts between different configurations. The $2p$ core-level width (4.95 eV in Re [63]) and apparative resolution also produce an additional broadening of the spectra.

The experimentally measured XAS and XMCD spectra at the Fe $L_{2,3}$ edges are available in the literature only for the BFRO compound [10]. Figure 9 presents the calculated XAS and XMCD spectra at the Fe $L_{2,3}$ edges in the BFRO oxide together with the experimental spectra [10]. Theory describes relatively well the shape and relative intensities of the x-ray absorption at the Fe $L_{2,3}$ edges in BFRO (upper panel of Fig. 9). The XMCD spectrum at the Fe L_3 edge possesses a strong negative peak at around 709 eV and a high-energy positive shoulder. The energy band-structure calculations well reproduce the major negative peak, but they do not completely describe the high-energy positive peak.

To address the magnetism in the earth alkaline ions themselves, which are usually neglected in the magnetic scenario, we present in Fig. 10 the XAS and XMCD theoretical spectra of BFRO at the Ba $L_{2,3}$ edges in comparison with the experimental ones [31]. Ba $5d$ states are almost empty in the BFRO oxide, and the Ba $L_{2,3}$ XAS and XMCD spectra occupy quite a large energy interval up to 50 eV. Theory well reproduces the major peaks both in the x-ray absorption and XMCD up to 20 eV above the $L_{2,3}$ edges. However, above this energy interval it fails to describe the fine structure of the spectra, partly due to the linear character of the LMTO method.

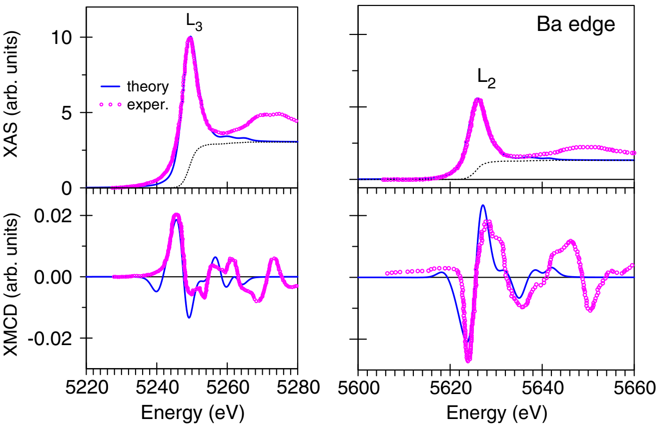

FIG. 10. The experimental x-ray-absorption and XMCD spectra (open circles) at the Ba $L_{2,3}$ edges in BFRO measured at 10 K with a 5 T magnetic field [31] compared with the theoretically calculated ones.

B. Fe, Ca, and O *K* XAS and XMCD spectra

The XAS and XMCD spectra in metals and alloys at the K edge in which $1s$ core electrons are excited to p-states through the dipole transitions are quite important. They are sensitive to the electronic states at neighboring sites because of the delocalized nature of valence p-states.

The XAS at the Fe K edge in the AFRO (A = Ba, Sr, and Ca) samples was measured at 40 K by Herrero-Martin *et al.* (Ref. [28]). Figure 11 shows the Fe K XAS and XMCD calculated spectra together with the experimental data. The XAS spectra of AFRO oxides are quite structured, showing well-defined features. The main traits of these spectra are a strong resonance at the threshold (denoted as c in Fig. 11), some low-energy prepeak structures denoted as a and b, and shoulders above the threshold (d and e). The c and d structures are ascribed to dipole $1s \rightarrow 4p$ transitions whose shape and intensity are related to local geometrical characteristics such as the scattering power of the A atom. In this way, Ba- and Ca-based samples show a strong c resonance while the weakest one corresponds to the SFRO compound. The feature a, which is well pronounced for the SFRO, was ascribed to $1s \rightarrow 3d$ quadrupole transitions in Ref. [28]. However, from our calculations this feature can be described well in the dipole approximation. Theory well describes the intensity of the shoulder b in CFRO, overestimates it in SFRO, and underestimates it in BFRO. The shoulders d are well described by theory in the SFRO and CFRO oxides. The shoulder c is seen only in CFRO.

The lower panel of Fig. 11 shows the Fe K theoretically calculated XMCD spectra. The shape and relative intensities of the fine structures are quite different in all three oxides. Experimental measurements of the Fe K XMCD spectra are highly desired.

Figure 12 presents the experimental x-ray-absorption (upper panel) and XMCD spectra (lower panel) (open circles) at the Ca K edge in CFRO [31] compared with the theoretically calculated ones. Theory well reproduces almost all of the fine structures of the x-ray-absorption spectrum, which consists of a major peak at 4048 eV and two low-energy peaks at 4039 and 4044 eV as well as a wide high-energy shoulder situated between 4056 and 4064 eV. Theory was not able, however, to reproduce the high-energy shoulder of the major peak at around 4051 eV.

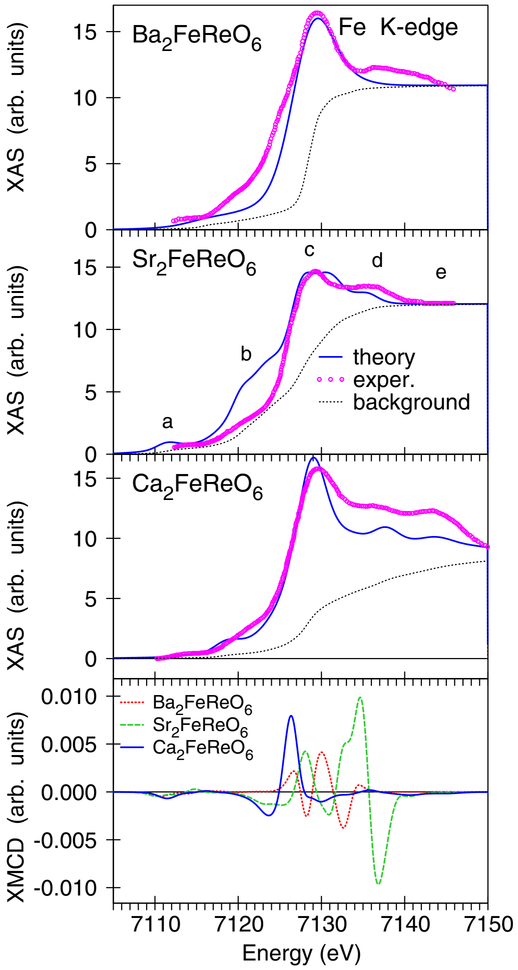

FIG. 11. The x-ray-absorption spectra (open circles) at Fe K edges in BFRO, SFRO, and CFRO [28] compared with the theoretically calculated ones. The lower panel presents the theoretically calculated Fe K XMCD spectra in these oxides.

The calculated $4p$ spin and orbital magnetic moments at the Ca site were equal to $M_s = -0.0012\,\mu_B$ and $M_l = -0.0022\,\mu_B$. Due to a small Ca $4p$ orbital moment, the corresponding Ca K XMCD spectrum has relatively small but well pronounced intensity (lower panel of Fig. 12). The major negative peak is in close vicinity to the Ca K edge at 4037 eV. There are several positive and negative peaks above 4042 eV. The theoretical calculations well describe the shape and intensity of the major negative peak and other high-energy fine structures. Figure 12 also presents the calculated x-ray linear dichroism (XLD) spectrum, which is obtained as a difference in the x-ray absorption for the linearly polarized x-ray light oriented parallel and perpendicular to the c axis. The latter spectrum is more than one order of magnitude larger than the XMCD one. In addition, the XLD spectrum has a very small signal near the Ca K edge where the XMCD spectrum has the major peak. Experimental measurements of the Ca K XLD spectrum are highly desired.

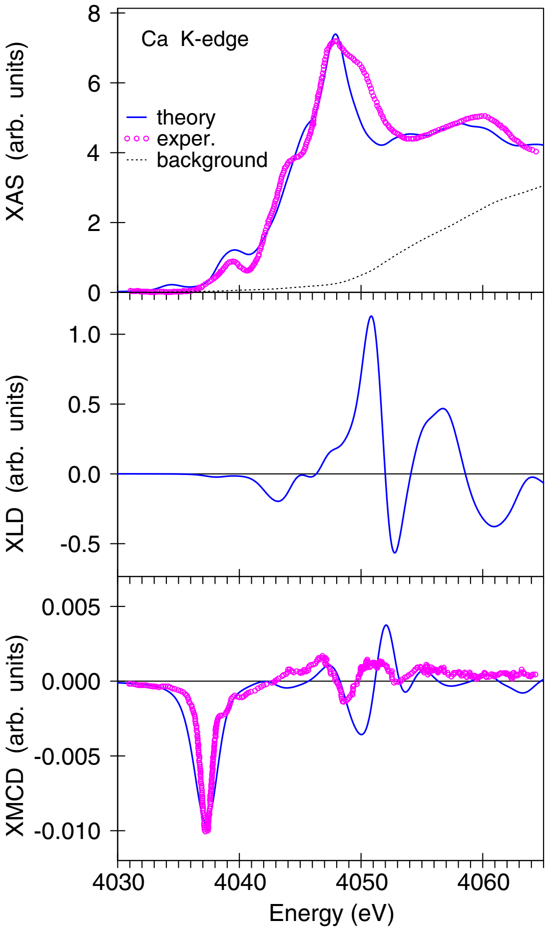

FIG. 12. The experimental x-ray-absorption (upper panel), XLD (middle panel), and XMCD spectra (lower panel) (open circles) at the Ca K edge in CFRO [31] compared with the theoretically calculated ones.

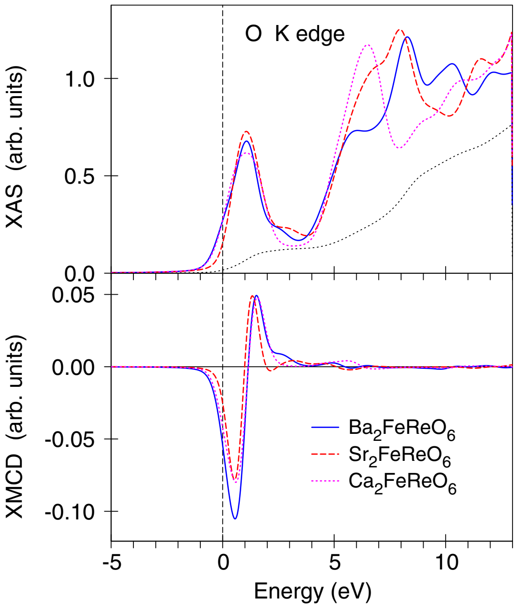

FIG. 13. The theoretically calculated x-ray-absorption (upper panel) and XMCD spectra (lower panel) at the O K edge in AFRO (A = Ba, Sr, and Ca).

Figure 13 presents the theoretically calculated x-ray absorption (upper panel) and XMCD spectra (lower panel) at the O K edge in AFRO oxides. The O K XAS spectra of the AFRO oxides are quite structured, showing well-defined features. The main features of these spectra are a strong resonance at the threshold and some high-energy peaks followed by a low minimum. The spectral features just above the threshold are attributed mainly to oxygen $2p$ empty orbitals hybridized with Re $5d$ and Fe $3d$ orbitals. The fine structures situated between 5 and 15 eV are due to O $2p$ orbitals hybridized with Fe $4s$ and $4p$ and Re $6s$ and $6p$ orbitals.

The dichroism at the O K edge is significant only for $2p$ states, which strongly hybridize with Re $5d$ and Fe $3d$ states at the 0–4 eV energy interval [see Fig. 13 (lower panel)]. The spectral XMCD features between 5 and 15 eV, which are due to O $2p$ orbitals hybridized with Re and Fe s and p orbitals, are extremely small.

C. Magnetic moments

In magnets, the spin M_s and orbital M_l magnetic moments are basic quantities, and their separate determination is therefore important. Methods of their experimental determination include traditional gyromagnetic ratio measurements [102], magnetic form-factor measurements using neutron scattering [103], and magnetic x-ray scattering [104]. In addition to these, the recently developed x-ray magnetic circular dichroism combined with several sum rules [53,54] has attracted much attention as a method of site- and symmetry-selective determination of M_s and M_l. Tables III and IV present a comparison between calculated and experimental magnetic moments in BFRO, SFRO, and CFRO at the Fe and Re sites, respectively.

The experimental magnetization values in the AFRO oxides measured below 4 K are equal to 3.27μ_B/f.u., 3.23μ_B/f.u., and 3.12μ_B/f.u. for A = Ba, Sr, and Ca, respectively [8]. Our theoretical results are in good agreement with the experiment, and they are equal to 3.260μ_B/f.u., 3.256μ_B/f.u., and 3.136μ_B/f.u. for A = Ba, Sr, and Ca, respectively, in the LSDA+U approximation.

TABLE III. The theoretically calculated and experimentally measured spin M_s and orbital M_l magnetic moments (in μ_B) at the Fe site of BFRO, SFRO, and CFRO.

	BFRO		SFRO		CFRO	
Method	M_s	M_l	M_s	M_l	M_s	M_l
LSDA	3.829	0.070	3.375	0.051	3.679	0.086
LSDA+U	4.016	0.084	3.943	0.079	3.969	0.109
Expt. [10] (XMCD)	2.8	0.04				
Expt. [10] (ND)	3.16	0.04				
Expt. [17]					4.0	
Theory [23]					3.87	
Theory [27]	4.01	0.04				
Theory [12]	4.16					

TABLE IV. The theoretically calculated and the experimentally measured spin M_s and orbital M_l magnetic moments (in μ_B) using XMCD, ND, and NMR experiments at the Re site of BFRO, SFRO, and CFRO (sum rules applied for the theoretically calculated XMCD spectra in the LSDA+U approximation).

	BFRO		SFRO		CFRO	
Method	M_s	M_l	M_s	M_l	M_s	M_l
LSDA	−0.768	0.155	−0.734	0.181	−0.753	0.336
LSDA+U	−0.829	0.199	−0.881	0.243	−1.108	0.662
Sum rules	−0.866	0.189	−1.007	0.213	−1.018	0.560
Expt. [31] (XMCD)	−0.56	0.15	−0.74	0.21	−0.47	0.16
Expt. [29] (XMCD)	−0.99	0.28	−1.07	0.74	−1.15	0.39
Expt. [10] (XMCD)	−0.64	0.19				
Expt. [105] (NMR)	−0.87		−0.94		−0.95	
Expt. [17] (ND)					−1.02	
Theory [23]	−0.41				−1.12	
Theory [27]	−1.04	0.38				
Theory [12]	−1.22					

The Fe spin and orbital moments are parallel, whereas the spin and orbital Re moments are antiparallel in the AFRO oxides, in accordance with Hund's third rule. Our LSDA calculated orbital magnetic moments for Fe and Re are lower than the results of the LSDA+U approach (Tables III and IV). It should be mentioned that the effect of the Coulomb correlations changes the energy band structure of transition-metal compounds in two ways. First, d occupied states are shifted downward by $U_{\text{eff}}/2$ and empty d states are shifted upward by this amount relative to the Fermi energy. Second, the Coulomb correlations enhance an effective spin-orbit coupling constant [106].

The LSDA+U Fe spin moment of $4.016\mu_B$ is in good agreement with the previous calculations in BFRO [12,27]. However, our orbital Fe magnetic moment in BFRO is larger than the results of Wang *et al.* [27], as well as the experimental data [10]. The LSDA+U Re spin moment of $-1.108\,\mu_B$ for CFRO is in good agreement with the experimental measurements using nuclear magnetic resonance (NMR) [105] and neutron diffraction (ND) [17] methods as well as with the theoretical results of Szotek *et al.* (Ref. [23]). Also, our orbital Re magnetic moment in BFRO is close to the experimental data [10,29]. Our calculated Re spin magnetic moment in BFRO is smaller than the results of Wu [12] and Wang *et al.* [27]. The results from different calculations may vary somewhat since the calculated moments depend on the details of the calculations and especially on the sizes of the muffin-tin spheres, which usually differ from each other for different calculations.

It is interesting to note that the spin magnetic moment of Fe calculated with LSDA+U is essentially constant over the series of compounds, despite the increased correlation effect. The orbital moment seems instead largest for the CFRO, where the value of U is the largest. We can conclude that the orbital moments are more sensitive to the correlation effects than the spin moments.

Tables III and IV also present the Fe and Re magnetic moments obtained from the XMCD experiments. In these experiments, the spin and orbital magnetic moments were obtained by using the XMCD sum rules [53,54], which relate the integrated signals over the spin-orbit split core edges of the circular dichroism to ground-state orbital and spin magnetic moments.

Because of the significant implications of the sum rules, numerous experimental and theoretical studies aimed at investigating their validity for itinerant magnetic systems have been reported, but with widely different conclusions. The claimed adequacy of the sum rules varies from very good (within 5% agreement) to very poor (up to 50% discrepancy) [50]. This lack of a consensus may have several origins. On the experimental side, the indirect x-ray-absorption techniques, i.e., the total electron and fluorescence yield methods, are known to suffer from saturation and self-absorption effects that are very difficult to correct for [107]. The total electron yield method can be sensitive to the varying applied magnetic field, changing the electron detecting efficiency, or, equivalently, the sample photocurrent. The fluorescence yield method is insensitive to the applied field, but the yield is intrinsically not proportional to the absorption cross section, because the radiative to nonradiative relative core-hole decay probability depends strongly on the symmetry and spin polarization of the XAS final states [108]. On the theoretical side, it has been demonstrated by circularly polarized $2p$ resonant photoemission measurements of Ni that both the band-structure effects and electron-electron correlations are needed to satisfactorily account for the observed XMCD spectra [109]. However, it is extremely difficult to include both of them in a single theoretical framework. In addition, XMCD sum rules are derived within an ionic model using a number of approximations. For $L_{2,3}$, they are as follows [110]: (i) ignoring the exchange splitting of the core levels; (ii) replacing the interaction operator $\boldsymbol{\alpha} \cdot \mathbf{a}_\lambda$ in Eq. (2) by $\nabla \cdot \mathbf{a}_\lambda$; (iii) ignoring the asphericity of the core states; (iv) ignoring the difference of $d_{3/2}$ and $d_{5/2}$ radial wave functions; (v) ignoring $p \rightarrow s$ transitions; and (vi) ignoring the energy dependence of the radial matrix elements.

To investigate a possible error of the sum rules, we compare the spin and orbital moments obtained from the theoretically calculated XAS and XMCD spectra through the sum rules with directly calculated LSDA+U values in order to avoid additional experimental problems. The sum rules [Eqs. (4) and (5)] reproduce the spin magnetic moments at the Re site within 4%, 12%, and 10% and the orbital moments within 5%, 12%, and 15% for the Ba-, Sr-, and Ca-based oxides, respectively (Table IV). Note that two independent XMCD measurements (Refs. [29] and [31]) produce quite different values of spin and orbital magnetic moments. The largest difference is up to 59% for spin moments in CFRO and even reaches 72% for orbital moments in SFRO (Table IV). Such large differences might be due to different sample quality and different experimental conditions.

Finally, our calculations produce induced spin and orbital magnetic moments at the oxygen site in BFRO of about $0.036\mu_B$ and $0.003\mu_B$, respectively. Two nonequivalent oxygen atoms in SFRO have $M_s^{\text{O}_1} = 0.045\,\mu_B$, $M_s^{\text{O}_2} = 0.044\mu_B$, $M_l^{\text{O}_1} = 0.021\mu_B$, and $M_l^{\text{O}_2} = -0.010\,\mu_B$. The magnetic moments in CFRO at the oxygen sites are equal to $M_s^{\text{O}_1} = 0.032\mu_B$, $M_s^{\text{O}_2} = 0.057\mu_B$, $M_s^{\text{O}_3} = 0.071\mu_B$, and $M_l^{\text{O}_1} = -0.010\mu_B$, $M_l^{\text{O}_2} = -0.011\mu_B$, $M_l^{\text{O}_3} = 0.041\mu_B$.

The calculated $5d$ spin and orbital magnetic moments at the Ba site were found to be equal to $M_s = -0.021\mu_B$ and $M_l = -0.006\mu_B$. The experimental magnetic moments from the XMCD measurements [31] estimated using the sum rules are $M_s^{\text{exp}} = -0.006\mu_B$ and $M_l^{\text{exp}} = -0.001\mu_B$. These values are significantly smaller than our theoretical results. This may be partly due to restriction of the sum rules. If we apply the sum rules to the theoretically calculated XMCD spectra, we also obtain reduced values of the magnetic moments at the Ba site: $M_s^{\text{sum rules}} = -0.003\,\mu_B$, $M_l^{\text{sum rules}} = -0.002\mu_B$.

V. CONCLUSIONS

A systematic electronic structure study of AFRO (A = Ba, Sr, and Ca) has been performed by employing LSDA and LSDA+U approximations in a frame of the fully relativistic spin-polarized Dirac LMTO band-structure method. We investigated the effects of the subtle interplay among SO coupling, electron correlation, and lattice distortion on the electronic structure of double perovskites. BFRO has very little lattice distortion, and the electronic structure is mainly determined by the SO coupling and to lesser extent by correlations. In contrast, CFRO has a large distortion in the Fe-O-Re bond, and the electronic structure is mainly determined by Coulomb electron correlations and lattice distortion. In the Ba-Sr-Ca row, the correlation effects are increased at the Fe site. The correlations at the Re site are small in the Ba- and Sr-based compounds but significant in CFRO. The latter compound behaves as an insulator only if considered with a relatively large value of Coulomb repulsion $U_{\text{eff}} = 2.3$ eV at the Re site in addition to $U_{\text{eff}} = 3.1$ eV at the Fe site.

We found that the spin and orbital magnetic moments in CFRO are changed linearly with temperature before and after the MIT and abruptly at the point of the phase transition. This jump is different for different sites. The easy axis of magnetization for the LT phase is along the b direction, in agreement with experimental data. For the HT phase, the MAE $K = E_{\langle 010\rangle} - E_{\langle 001\rangle}$ is extremely small with a barrier in between, so even a slight degree of chemical disorder and inhomogeneity may change the easy axis of magnetization between $\langle 010\rangle$ and $\langle 001\rangle$ directions. The orbital magnetic anisotropy is four times larger than the spin magnetic anisotropy for both sites. The major contribution to the MAE is due to the orbital magnetic anisotropy at the Re site.

The x-ray-absorption spectra and x-ray magnetic circular dichroism at the Re, Fe, and Ba $L_{2,3}$ edges and Fe, Ca, and O K edges were investigated theoretically in the frame of the LSDA+U method. The theory describes relatively well the shape and relative intensities of the x-ray-absorption and XMCD spectra in AFRO oxides. The experimentally measured dichroic Re L_2 line consists of an intensive asymmetric negative peak in all three compounds. The XMCD at the Re L_3 edge has three peaks: two positive high-energy peaks and one lower-energy negative peak. A qualitative explanation of Re $L_{2,3}$ XMCD spectra is provided by the analysis of the corresponding selection rules, orbital character, and occupation numbers of individual $5d$ orbitals. We show that the XMCD spectra at the Re L_2 edge can be roughly approximated by the following sum of m_j-projected partial densities of states: $-(N^{3/2}_{1/2} + N^{3/2}_{3/2})$. As a result, the shape of the Re L_2 XMCD spectra contains an asymmetric negative peak. The Re L_3 XMCD spectra can be approximated by $(N^{5/2}_{-5/2} + N^{5/2}_{-3/2}) - N^{3/2}_{3/2}$. This expression explains why the L_3 XMCD spectra have two positive peaks and one negative peak. The relative intensity of these peaks is strongly changed going from Ba to Ca oxides. The high-energy positive peak is the largest in BFRO and becomes smaller in SFRO and CFRO. The low-energy negative peak is the smallest in BFRO and increases significantly in CFRO. The latter can be explained by a decrease of the Re $5d_{3/2}$ occupation number in the Ba-Sr-Ca row, and, hence, an increase in the number of empty $5d_{3/2}$ states (an increase in the contribution from the negative $-N^{3/2}_{3/2}$ term).

ACKNOWLEDGMENTS

We are thankful to A. N. Yaresko for helpful discussions. V.N.A. gratefully acknowledges the hospitality at Max-Planck-Institut für Mikrostrukturphysik in Halle during his stay there. This work was supported by Science and Technology Center in Ukraine STCU, Project No. 6255.

---

[1] M. Ziese, Rep. Prog. Phys. **65**, 143 (2002).

[2] K. I. Kobayashi, T. Kimura, H. Sawada, K. Terakura, and Y. Tokura, Nature (London) **395**, 357 (1998).

[3] H. Kato, T. Okuda, Y. Okimoto, Y. Tomioka, K. Oikawa, T. Kamiyama, and Y. Tokura, Phys. Rev. B **69**, 184412 (2004).

[4] J. M. D. Coey, Adv. Phys. **48**, 167 (1999).

[5] D. Serrate, J. M. D. Teresa, and M. R. Ibarra, J. Phys.: Condens. Matter **19**, 023201 (2007).

[6] H. Kato, T. Okuda, Y. Okimoto, Y. Tomioka, Y. Takenoya, A. Ohkubo, M. Kawasaki, and Y. Tokura, Appl. Phys. Lett. **81**, 328 (2002).

[7] T. Alamelu, U. V. Varadaraju, M. Venkatesan, A. P. Douvalis, and J. M. D. Coey, J. Appl. Phys. **91**, 8909 (2002).

[8] J. M. Michalik, J. M. D. Teresa, J. Blasco, P. A. Algarabel, M. R. Ibarra, C. Kapusta, and U. Zeitler, J. Phys.: Condens. Matter **19**, 506206 (2007).

[9] W. Prellier, V. Smolyaninova, A. Biswas, C. Galley, R. Greene, K. Ramesha, and J. Gopalakrishnan, J. Phys.: Condens. Matter **12**, 965 (2000).

[10] C. Azimonte, J. C. Cezar, E. Granado, Q. Huang, J. W. Lynn, J. C. P. Campoy, J. Gopalakrishnan, and K. Ramesha, Phys. Rev. Lett. **98**, 017204 (2007).

[11] K.-I. Kobayashi, T. Kimura, Y. Tomioka, H. Sawada, K. Terakura, and Y. Tokura, Phys. Rev. B **59**, 11159 (1999).

[12] H. Wu, Phys. Rev. B **64**, 125126 (2001).

[13] H.-T. Jeng and G. Y. Guo, Phys. Rev. B **67**, 094438 (2003).

[14] K. Oikawa, T. Kamiyama, H. Kato, and Y. Tokura, J. Phys. Soc. Jpn. **72**, 1411 (2003).

[15] J. M. DeTeresa, D. Serrate, J. Blasco, M. R. Ibarra, and L. Morellon, Phys. Rev. B **69**, 144401 (2004).

[16] J. Gopalakrishnan, A. Chattopadhyay, S. B. Ogale, T. Venkatesan, R. L. Greene, A. J. Millis, K. Ramesha,

B. Hannoyer, and G. Marest, Phys. Rev. B **62**, 9538 (2000).
[17] W. Westerburg, O. Lang, C. Ritter, C. Felser, W. Tremel, and G. Jakob, Solid State Commun. **122**, 201 (2002).
[18] Z. Szotek, W. M. Temmerman, A. Svane, L. Petit, and H. Winter, Phys. Rev. B **68**, 104411 (2003).
[19] H. Iwasawa, T. Saitoh, Y. Yamashita, D. Ishii, H. Kato, N. Hamada, Y. Tokura, and D. D. Sarma, Phys. Rev. B **71**, 075106 (2005).
[20] B. Fisher, J. Genossar, K. B. Chashka, L. Patlagan, and G. M. Reisner, J. Magn. Magn. Mater. **316**, e713 (2007).
[21] E. Granado, Q. Huang, J. W. Lynn, J. Gopalakrishnan, R. L. Greene, and K. Ramesha, Phys. Rev. B **66**, 064409 (2002).
[22] J. M. Wills, O. Eriksson, M. Alouani, and O. L. Price, *Electronic Structure and Physical Properties of Solids* (Springer, Berlin, 2000).
[23] Z. Szotek, W. M. Temmerman, A. Svane, L. Petit, G. M. Stocks, and H. Winter, J. Magn. Magn. Mater. **272-276**, 1816 (2004).
[24] G. Vaitheeswaran, V. Kanchana, and A. Delin, J. Phys.: Conf. Ser. **29**, 50 (2006).
[25] J. I. Melo and R. Weht, Physica B **404**, 2754 (2009).
[26] B. C. Jeon, C. H. Kim, S. J. Moon, W. S. Choi, H. Jeong, Y. S. Lee, J. Yu, C. J. Won, J. H. Jung, N. Hur *et al.*, J. Phys.: Condens. Matter **22**, 345602 (2010).
[27] J. Wang, N. N. Zu, Y. Wang, and Z. J. Wu, J. Magn. Magn. Mater. **339**, 163 (2013).
[28] J. Herrero-Martin, G. Subias, J. Blasco, J. Garcia, and M. C. Sanchez, J. Phys.: Condens. Matter **17**, 4963 (2005).
[29] M. Sikora, C. Kapusta, M. Borowiec, C. J. Oates, V. Prochazka, D. Rybicki, D. Zajac, J. M. D. Teresa, C. Marquina, and M. R. Ibarra, Appl. Phys. Lett. **89**, 062509 (2006).
[30] M. Sikora, O. Mathon, P. van der Linden, J. M. Michalik, J. M. de Teresa, C. Kapusta, and S. Pascarelli, Phys. Rev. B **79**, 220402(R) (2009).
[31] A. Winkler, N. Narayanan, D. Mikhailova, K. G. Bramnik, H. Ehrenberg, H. Fuess, G. Vaitheeswaran, V. Kanchana, F. Wilhelm, A. Rogalev *et al.*, New J. Phys. **11**, 073047 (2009).
[32] J. P. Clancy, N. Chen, C. Y. Kim, W. F. Chen, K. W. Plumb, B. C. Jeon, T. W. Noh, and Y.-J. Kim, Phys. Rev. B **86**, 195131 (2012).
[33] V. I. Anisimov, J. Zaanen, and O. K. Andersen, Phys. Rev. B **44**, 943 (1991).
[34] A. M. Glazer, Acta Crystallogr. B **28**, 3384 (1972).
[35] N. Autha, G. Jakoba, W. Westerburga, C. Ritterb, I. Bonnc, C. Felserc, and W. Tremel, J. Magn. Magn. Mater. **272-276**, e607 (2004).
[36] C. Hirjibehedin, C. Lin, A. Otte, M. Ternes, C. Lutz, and B. Jones, Science **317**, 1199 (2007).
[37] H. Brooks, Phys. Rev. **58**, 909 (1940).
[38] G. C. Fletcher, Proc. R. Soc. London, Ser. A **67**, 505 (1954).
[39] J. Trygg, B. Johansson, O. Eriksson, and J. M. Wills, Phys. Rev. Lett. **75**, 2871 (1995).
[40] S. V. Halilov, A. Y. Perlov, P. M. Oppeneer, A. N. Yaresko, and V. N. Antonov, Phys. Rev. B **57**, 9557 (1998).
[41] P. Ravindran, A. Delin, P. James, B. Johansson, J. M. Wills, R. Ahuja, and O. Eriksson, Phys. Rev. B **59**, 15680 (1999).
[42] G. H. O. Daalderop, P. J. Kelly, and M. F. H. Schuurmans, Phys. Rev. B **41**, 11919 (1990).
[43] D.-S. Wang, R. Wu, and A. J. Freeman, Phys. Rev. Lett. **70**, 869 (1993).
[44] V. N. Antonov, B. N. Harmon, A. N. Yaresko, L. V. Bekenov, and A. P. Shpak, Phys. Rev. B **73**, 094445 (2006).
[45] V. P. Antropov, V. N. Antonov, L. V. Bekenov, A. Kutepov, and G. Kotliar, Phys. Rev. B **90**, 054404 (2014).
[46] V. P. Antropov and V. N. Antonov, Phys. Rev. B **90**, 094406 (2014).
[47] J. Smit and H. P. J. Wijn, *Ferrites* (Philips Technical Library, Eindhoven, 1959).
[48] G. Y. Guo, H. Ebert, W. M. Temmerman, and P. J. Durham, Phys. Rev. B **50**, 3861 (1994).
[49] V. N. Antonov, A. I. Bagljuk, A. Y. Perlov, V. V. Nemoshkalenko, V. N. Antonov, O. K. Andersen, and O. Jepsen, Low Temp. Phys. **19**, 494 (1993).
[50] V. Antonov, B. Harmon, and A. Yaresko, *Electronic Structure and Magneto-Optical Properties of Solids* (Kluwer, Dordrecht, 2004).
[51] E. Arola, M. Horne, P. Strange, H. Winter, Z. Szotek, and W. M. Temmerman, Phys. Rev. B **70**, 235127 (2004).
[52] B. T. Thole and G. van der Laan, Phys. Rev. B **38**, 3158 (1988).
[53] B. T. Thole, P. Carra, F. Sette, and G. van der Laan, Phys. Rev. Lett. **68**, 1943 (1992).
[54] P. Carra, B. T. Thole, M. Altarelli, and X. Wang, Phys. Rev. Lett. **70**, 694 (1993).
[55] G. van der Laan and B. T. Thole, Phys. Rev. B **53**, 14458 (1996).
[56] V. N. Antonov, O. Jepsen, A. N. Yaresko, and A. P. Shpak, J. Appl. Phys. **100**, 043711 (2006).
[57] V. N. Antonov, A. N. Yaresko, and O. Jepsen, Phys. Rev. B **81**, 075209 (2010).
[58] O. K. Andersen, Phys. Rev. B **12**, 3060 (1975).
[59] V. V. Nemoshkalenko, A. E. Krasovskii, V. N. Antonov, V. N. Antonov, U. Fleck, H. Wonn, and P. Ziesche, Phys. Status Solidi B **120**, 283 (1983).
[60] V. N. Antonov, A. Y. Perlov, A. P. Shpak, and A. N. Yaresko, J. Magn. Magn. Mater. **146**, 205 (1995).
[61] S. Park, H. J. Ryu, S. B. Kim, B. W. Lee, and C. S. Kim, Physica B **345**, 99 (2004).
[62] P. E. Blöchl, O. Jepsen, and O. K. Andersen, Phys. Rev. B **49**, 16223 (1994).
[63] J. L. Campbell and T. Parr, At. Data Nucl. Data Tables **77**, 1 (2001).
[64] J. P. Perdew and A. Zunger, Phys. Rev. B **23**, 5048 (1981).
[65] L. Hedin, Phys. Rev. **139**, A796 (1965).
[66] W. Metzner and D. Vollhardt, Phys. Rev. Lett. **62**, 324 (1989).
[67] T. Pruschke, M. Jarell, and J. K. Freericks, Adv. Phys. **44**, 187 (1995).
[68] A. Georges, G. Kotliar, W. Krauth, and M. J. Rozenberg, Rev. Mod. Phys. **68**, 13 (1996).
[69] A. N. Yaresko, V. N. Antonov, and P. Fulde, Phys. Rev. B **67**, 155103 (2003).
[70] V. I. Anisimov and O. Gunnarsson, Phys. Rev. B **43**, 7570 (1991).
[71] I. V. Solovyev, P. H. Dederichs, and V. I. Anisimov, Phys. Rev. B **50**, 16861 (1994).
[72] P. H. Dederichs, S. Blügel, R. Zeller, and H. Akai, Phys. Rev. Lett. **53**, 2512 (1984).
[73] W. E. Pickett, S. C. Erwin, and E. C. Ethridge, Phys. Rev. B **58**, 1201 (1998).

[74] M. Cococcioni and S. de Gironcoli, Phys. Rev. B **71**, 035105 (2005).

[75] K. Nakamura, R. Arita, Y. Yoshimoto, and S. Tsuneyuki, Phys. Rev. B **74**, 235113 (2006).

[76] F. Aryasetiawan, M. Imada, A. Georges, G. Kotliar, S. Biermann, and A. I. Lichtenstein, Phys. Rev. B **70**, 195104 (2004).

[77] I. V. Solovyev and M. Imada, Phys. Rev. B **71**, 045103 (2005).

[78] F. Aryasetiawan, K. Karlsson, O. Jepsen, and U. Schonberger, Phys. Rev. B **74**, 125106 (2006).

[79] E. Antonides, E. C. Janse, and G. A. Sawatzky, Phys. Rev. B **15**, 1669 (1997).

[80] D. van der Marel, G. A. Sawatzky, and F. U. Hillebrecht, Phys. Rev. Lett. **53**, 206 (1984).

[81] See Supplemental Material at http://link.aps.org/supplemental/10.1103/PhysRevB.94.035122 for details regarding the set of Hubbard U parameters.

[82] A. R. Mackintosh and O. K. Andersen, in *Electrons at the Fermi Surface*, edited by M. Springford (Cambridge University Press, Cambridge, 1980), pp. 149–224.

[83] T. Saitoh, H. Iwasawa, H. Kato, Y. Tokura, N. Hamada, and D. Sarma, J. Electron. Spectrosc. Relat. Phenom. **144-147**, 337 (2005).

[84] E. Pavarini, A. Yamasaki, J. Nuss, and O. K. Andersen, New J. Phys. **7**, 188 (2005).

[85] M. Mochizuki and M. Imada, Phys. Rev. Lett. **91**, 167203 (2003).

[86] M. Mochizuki and M. Imada, J. Phys. Soc. Jpn. **73**, 1833 (2004).

[87] K. Yosida, A. Okiji, and S. Chikazumi, Prog. Theor. Phys. **33**, 559 (1965).

[88] M. Cinal, D. M. Edwards, and J. Mathon, Phys. Rev. B **50**, 3754 (1994).

[89] M. Montalti, A. Credi, L. Prodi, and M. T. Gandolfi, in *Handbook of Photochemistry*, edited by N. J. Turro (Taylor and Francis, Boca Raton, FL, 2006), p. 629.

[90] F. M. F. Groot, Physica B **208-209**, 15 (1995).

[91] O. Gunnarsson and K. S. Schönhammer, Phys. Rev. Lett. **50**, 604 (1983).

[92] J. Allen, S. Oh, O. Gunnarsson, K. Schönhammer, M. Maple, M. Torikachvili, and I. Lindau, Adv. Phys. **35**, 275 (1986).

[93] H. Matsuyama, I. Harada, and A. Kotani, J. Phys. Soc. Jpn. **66**, 337 (1997).

[94] K. Fukui, H. Matsuyama, I. Harada, J. C. Parlebas, and A. Kotani, J. Electron. Spectrosc. Relat. Phenom. **104**, 67 (1999).

[95] K. Asakura, K. Fukui, H. Ogasawara, I. Harada, J. C. Parlebas, and A. Kotani, J. Phys. Soc. Jpn. **73**, 2008 (2004).

[96] J. C. Parlebas and A. Kotani, J. Electron. Spectrosc. Relat. Phenom. **136**, 3 (2004).

[97] K. Asakura, A. Kotani, and I. Harada, J. Phys. Soc. Jpn. **74**, 1328 (2005).

[98] J. Parlebas, K. Asakura, A. Fujiwara, I. Harada, and A. Kotani, Phys. Rep. **431**, 1 (2006).

[99] T. Konishi, K. Morikawa, K. Kobayashi, T. Mizokawa, A. Fujimori, K. Mamiya, F. Iga, H. Kawanaka, Y. Nishihara, A. Delin *et al.*, Phys. Rev. B **62**, 14304 (2000).

[100] S. D. Brown, P. Strange, L. Bouchenoire, B. Zarychta, P. B. J. Thompson, D. Mannix, S. J. Stockton, M. Horne, E. Arola, H. Ebert *et al.*, Phys. Rev. Lett. **99**, 247401 (2007).

[101] V. N. Antonov, L. V. Bekenov, and V. P. Antropov, Phys. Rev. B **89**, 165110 (2014).

[102] G. G. Scott, J. Phys. Soc. Jpn. **17**, 372 (1962).

[103] W. Marshall and S. W. Lovsey, *Theory of Thermal Neutron Scattering* (Oxford University Press, Oxford, 1971).

[104] M. Blume, J. Appl. Phys. **57**, 3615 (1985).

[105] C. Kapusta, D. Zajac, P. C. Riedi, M. Sikora, C. J. Oates, J. Blasco, and M. R. Ibarra, J. Magn. Magn. Mater. **272–276**, e1619 (2004).

[106] G.-Q. Liu, V. N. Antonov, O. Jepsen, and O. K. Andersen, Phys. Rev. Lett. **101**, 026408 (2008).

[107] T. Böske, W. Clemens, C. Carbone, and W. Eberhardt, Phys. Rev. B **49**, 4003 (1994).

[108] C. T. Chen, Y. U. Idzerda, H.-J. Lin, N. V. Smith, G. Meigs, E. Chaban, G. H. Ho, E. Pellegrin, and F. Sette, Phys. Rev. Lett. **75**, 152 (1995).

[109] L. H. Tjeng, C. T. Chen, P. Rudolf, G. Meigs, G. van der Laan, and B. T. Thole, Phys. Rev. B **48**, 13378 (1993).

[110] H. Ebert, Rep. Prog. Phys. **59**, 1665 (1996).